



HAL
open science

Lithium-Rich Cobalt-Free Manganese-Based Layered Cathode Materials for Li-Ion Batteries: Suppressing the Voltage Fading

Ashraf Abdel-Ghany, Ahmed M Hashem, Alain Mauger, Christian M Julien

► **To cite this version:**

Ashraf Abdel-Ghany, Ahmed M Hashem, Alain Mauger, Christian M Julien. Lithium-Rich Cobalt-Free Manganese-Based Layered Cathode Materials for Li-Ion Batteries: Suppressing the Voltage Fading. *Energies*, 2020, 13 (13), pp.3487. 10.3390/en13133487. hal-02933721

HAL Id: hal-02933721

<https://hal.sorbonne-universite.fr/hal-02933721v1>



Submitted on 8 Sep 2020

HAL is a multi-disciplinary open access archive for the deposit and dissemination of scientific research documents, whether they are published or not. The documents may come from teaching and research institutions in France or abroad, or from public or private research centers.

L'archive ouverte pluridisciplinaire **HAL**, est destinée au dépôt et à la diffusion de documents scientifiques de niveau recherche, publiés ou non, émanant des établissements d'enseignement et de recherche français ou étrangers, des laboratoires publics ou privés.

Article

Lithium-Rich Cobalt-Free Manganese-Based Layered Cathode Materials for Li-Ion Batteries: Suppressing the Voltage Fading

Ashraf Abdel-Ghany ¹, Ahmed M. Hashem ¹, Alain Mauger ² and Christian M. Julien ^{2,*}

¹ Inorganic Chemistry Department, National Research Centre, Dokki-Giza 12622, Egypt; achraf_28@yahoo.com (A.A.-G.); ahmedh242@yahoo.com (A.M.H.)

² Institut de Minéralogie, Physique des Matériaux et Cosmologie (IMPMC), Sorbonne Université, CNRS UMR 7590, 4 Place Jussieu, CEDEX 05, 75252 Paris, France; alain.muager@sorbonne-universite.fr

* Correspondence: christian.julien@sorbonne-universite.fr

Received: 19 May 2020; Accepted: 3 July 2020; Published: 6 July 2020



Abstract: Lithium-rich layered oxides are recognized as promising materials for Li-ion batteries, owing to higher capacity than the currently available commercialized cathode, for their lower cost. However, their voltage decay and cycling instability during the charge/discharge process are problems that need to be solved before their practical application can be envisioned. These problems are mainly associated with a phase transition of the surface layer from the layered structure to the spinel structure. In this paper, we report the AlF₃-coating of the Li-rich Co-free layered Li_{1.2}Ni_{0.2}Mn_{0.6}O₂ (LLNMO) oxide as an effective strategy to solve these problems. The samples were synthesized via the hydrothermal route that insures a very good crystallization in the layered structure, probed by XRD, energy-dispersive X-ray (EDX) spectroscopy, and Raman spectroscopy. The hydrothermally synthesized samples before and after AlF₃ coating are well crystallized in the layered structure with particle sizes of about 180 nm (crystallites of ~65 nm), with high porosity (pore size 5 nm) determined by Brunauer–Emmett–Teller (BET) specific surface area method. Subsequent improvements in discharge capacity are obtained with a ~5-nm thick coating layer. AlF₃-coated Li_{1.2}Ni_{0.2}Mn_{0.6}O₂ delivers a capacity of 248 mAh g⁻¹ stable over the 100 cycles, and it exhibits a voltage fading rate of 1.40 mV per cycle. According to the analysis from galvanostatic charge-discharge and electrochemical impedance spectroscopy, the electrochemical performance enhancement is discussed and compared with literature data. Post-mortem analysis confirms that the AlF₃ coating is a very efficient surface modification to improve the stability of the layered phase of the Li-rich material, at the origin of the significant improvement of the electrochemical properties.

Keywords: Li-rich oxide; layered structure; cathode; voltage decay; Li-ion batteries

1. Introduction

The energy density (E in Wh g⁻¹) of a battery is determined by the amount of charge it can hold (Ah kg⁻¹) and by the voltage across its terminal (V); optimization of its electrochemical performance is achieved by an appropriate selection of anode and cathode materials [1]. In this context, layered Li-rich materials are attracting a lot of attention, because their capacity is the best among the lithium intercalation materials. In addition, they are not expensive and non-toxic when they are cobalt-free. Layered lithium-rich cobalt-free manganese-based oxides (LLNMOs) have been widely considered as new cathode materials for Li-ion batteries [2–40]. They are constituted by the architectural solid solution $y\text{Li}_2\text{MnO}_3(1-y)\text{LiMO}_2$ ($M = \text{Mn}, \text{Ni}$), which includes the monoclinic Li₂MnO₃ ($C2/m$ space group) and the rhombohedral LiMO₂ ($R\bar{3}m$ space group) phase. Both $R\bar{3}m$ and $C2/m$ phases have a

layered structure with a repeating transition-metal layer, oxygen layer, and lithium layer as shown in Figure 1 [2]. The high specific capacity ($>250 \text{ mAh g}^{-1}$) with an average discharge voltage of $>3.5 \text{ V}$ vs. Li^+/Li and the high energy density approaching 1000 Wh kg^{-1} are due to the activation of the Li_2MnO_3 component at potential $>4.4 \text{ V}$ vs. Li^+/Li during the first charge and the structural stability due to the Mn-rich composition. The early work by Lu et al. [3,4] demonstrated the stable reversible capacity in the potential window 2.0–4.6 V of the series $\text{Li}_{4/3-2x/3}\text{Ni}_x\text{Mn}_{2/3-x/3}\text{O}_2$, in which $\text{Li}_{1.11}\text{Ni}_{0.33}\text{Mn}_{0.56}\text{O}_2$ ($x = 0.33$) exhibited a specific capacity of $\sim 230 \text{ mAh g}^{-1}$. Then Kang et al. [5] reported the strong correlation between structure and electrochemical performance. Among various LLNMO compositions, $\text{Li}_{1.5}\text{Ni}_{0.25}\text{Mn}_{0.75}\text{O}_{2.5}$ ($\text{Li}_{1.2}\text{Ni}_{0.2}\text{Mn}_{0.6}\text{O}_2$ or $0.5\text{Li}_2\text{MnO}_3 \cdot 0.5\text{LiNi}_{0.5}\text{Mn}_{0.5}\text{O}_2$ in layered notation) has attracted much interest because it is also considered as an inter-grown composite; this Co-free structure exhibited the lowest voltage decay rate [6] and was easily synthesized by wet-chemical methods.

In spite of the efforts to obtain good reproducible electrochemical performance, practical applications of LLNMOs are still hindered by a large irreversible capacity loss in the initial cycle, severe capacity and voltage fading during long-term cycling, and poor rate capability [7,8]. Upon successive charge-discharge reactions, a surface reconstruction layer (SRL) occurs, which directly correlates to the electrochemical performance of the electrode. The SRL features are as follows: (1) creation of oxygen vacancies; (2) migration of transition metal (TM) cations into Li-sites; (3) reduction of the TM cations to low valence state; and (4) transformation of the lattice structure [9,10]. Zheng et al. [11] evidenced the influence of the synthesis conditions on the voltage decay rate, concluding that the sol-gel method provides better performance than the co-precipitation technique. It has been suggested that one of the main reasons for voltage fade is the irreversible migration of TM to the Li layer promoted by oxygen vacancies [12].

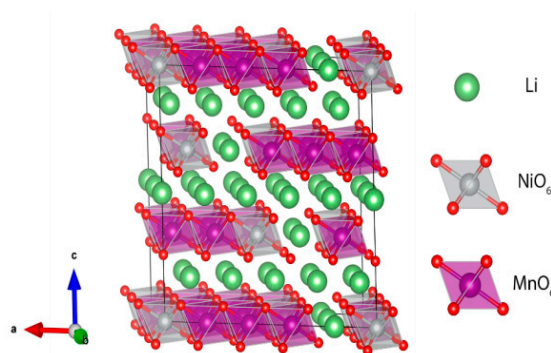


Figure 1. Schematic view of the crystal structure of Li-rich $\text{Li}_{1.2}\text{Ni}_{0.2}\text{Mn}_{0.6}\text{O}_2$. The red, green, silver, and purple spheres represent O, Li, Ni, and Mn atoms, respectively. Reproduced with permission from [2]. Copyright 2018 Wiley.

Several strategies have been employed to enhance the electrochemical properties of any cathode materials and reduce the voltage decay rate upon long-term cycling. The first approach is surface modification, since the coat can protect the active particles against corrosion and dissolution, and improve the electrical contact between powders (for a review, see [1]). Various substances have been deposited on the surface of active particles such as Li^+ -conductor (Li_2ZrO_3 , LiAlO_2) [13,14], inert compound (AlF_3 , Al_2O_3) [15], wide-gap semiconductor (ZnO) [16], and carbon [17,18]. $\text{Li}_{1.2}\text{Ni}_{0.2}\text{Mn}_{0.6}\text{O}_2$ nanoparticles (100–200 nm in size) coated with a thin layer of Li_2ZrO_3 obtained through a synchronous lithiation strategy delivered a capacity of circa 169 mAh g^{-1} over 100 cycles at current density 200 mA g^{-1} [13]. ZnO coating also improved the electrochemical properties of $0.5\text{Li}_2\text{MnO}_3 \cdot 0.5\text{LiNi}_{0.5}\text{Mn}_{0.5}\text{O}_2$; a specific discharge capacity of 215 mAh g^{-1} was reported after 10 cycles for ZnO treated LLNMO against 181 mAh g^{-1} for pristine electrode [19]. Enhanced electrochemical properties were observed for $\text{Li}_{1.2}\text{Ni}_{0.2}\text{Mn}_{0.6}\text{O}_2$ synthesized nickel enrichment is a second way to mitigate the voltage fading. For example, Shi et al. [20] demonstrated that Ni ions act as stabilizing ions to inhibit the Jahn–Teller effect of active Mn^{3+} ions in $0.5\text{Li}_2\text{MnO}_3 \cdot 0.5\text{LiNi}_{0.8}\text{Co}_{0.1}\text{Mn}_{0.1}\text{O}_2$. Doping or

cationic substitution is another successful method to reduce the voltage drop [21,22]. Substitution of a small amount of M^{3+} ($M = \text{Al, Cr, Fe, Co}$) for Mn^{4+} and Ni^{2+} in $\text{Li}(\text{Li}_{0.2}\text{Mn}_{0.6}\text{Ni}_{0.2})\text{O}_2$ sensitively influences the length of the plateau region due to the changes in the metal–oxygen bond covalence [23]. Ba doping improves the first-cycle Coulombic efficiency of $\text{Li}_{1.2}\text{Mn}_{0.6}\text{Ni}_{0.2}\text{O}_2$ by mitigating the oxidation of O^{2-} ions [24]. The synergetic effects of coating and doping were used by Liu et al. who synthesized $\text{Li}_{1.2}\text{Ni}_{0.2}\text{Mn}_{0.6}\text{O}_2$ by co-precipitation technique with 3 wt.% LiAlO_2 coat and 0.8% Cr doping [14]: (i) the spinel phase was suppressed, (ii) the midpoint voltage increased from 2.746 to 3.128 V, and (iii) higher D_{Li} contributed to good rate capability. Nevertheless, even though doping was able to significantly improve the electrochemical performance of the material, it did not solve the problem of side reactions with the electrolyte, dissolution, and phase transition of the surface layer to the spinel phase. Surface modification remains mandatory. However, the efficiency of the coating is also debated, because it depends on several parameters, including full surface coverage, thickness of the coating layer, the composition of the coat, and the morphology of the particles. This last parameter also plays an important role. In particular, use of nano-sized particles is needed for any cathode element to shorten the diffusion path. However, in the particular case of the $\alpha\text{-NaFeO}_2$ structure of $\text{Li}_{1.2}\text{Ni}_{0.2}\text{Mn}_{0.6}\text{O}_2$ considered here, it is also necessary to increase the size of the active (010) lattice planes at the surface.

As an experimental fact, the crystal morphology of LLNMOs and subsequent electrochemical performance are strongly dependent on the synthesis technique. Many methods have been tested to prepare “optimized” $\text{Li}_{1.2}\text{Ni}_{0.2}\text{Mn}_{0.6}\text{O}_2$ powders such as the solid state reaction [17,25], sol-gel process [15,26], co-precipitation method [27–29], combustion process [30,31], sol-freeze-drying method [32], ball-milling [33], hydrothermal [34–37], templating process [38], microwave heating process [39,40], and lithium ion-exchange reaction [41]. Currently, well-crystallized LLNMO materials prepared via wet-chemical synthesis are subjected to post-annealing treatment, i.e., typically a two-step calcination at $\sim 350/900$ °C for 10/4 h in air [36,42–44]. Among these methods, the co-precipitation process is a widely used synthesis approach to obtain spherical and mono-dispersed materials [45]. However, prolonged post-treatment provide big particles that limit the rate capability. Liu et al. [35] revealed the influence of the synthesis techniques on the voltage fading rate in the $\text{Li}_{1.2}\text{Ni}_{0.2}\text{Mn}_{0.6}\text{O}_2$ electrode, with a decrease of this rate in the sequence co-precipitation > sol-gel > hydrothermal method. Therefore, hydrothermal synthesis seems to be the best synthesis route.

In the present work, the voltage decay in long-term cycled $\text{Li}_{1.2}\text{Ni}_{0.2}\text{Mn}_{0.6}\text{O}_2$ is investigated for pristine and AlF_3 -coated samples. AlF_3 has been chosen as the inert material to coat the particles. The hydrothermal method has been chosen not only to minimize the fading rate, but also because it is well suited for the preparation of nano-sized powders with a spherical-like shape that is considered as the best morphology to optimize the electrochemical properties. The structure and morphology of the as-prepared sample are analyzed by X-ray diffraction (XRD), Raman spectroscopy, Brunauer–Emmett–Teller (BET) specific surface area method, scanning electron microscopy (SEM), and high-resolution transmission electron microscopy (HRTEM). Electrochemical properties are studied using galvanostatic charge-discharge (GCD) and electrochemical impedance spectroscopy (EIS) experiments. Chemical diffusion coefficients of Li^+ ions in LLNMO lattices are evaluated. Finally, the rate capability and cycle ability of LLNMO electrodes are further investigated and discussed. As a result, importantly, both the rate capability and cycle ability have been improved, with a capacity of 248 mAh g^{-1} stable over the 100 cycles. Moreover, the voltage fading rate has been reduced to 1.40 mV per cycle. These results prove the efficiency of the AlF_3 coating to protect the surface layer of the Li-rich particles.

2. Materials and Methods

2.1. Preparation of $\text{Li}_{1.2}\text{Ni}_{0.2}\text{Mn}_{0.6}\text{O}_2$ Nanoparticles

Li-rich layered $\text{Li}_{1.2}\text{Ni}_{0.2}\text{Mn}_{0.6}\text{O}_2$ powders were prepared by a two-step process, i.e., a hydrothermal synthesis followed by a solid-state calcination. Lithium and transition-metal (TM) acetates (analytical grade from Merck KGaA, Darmstadt, Germany) were mixed in distilled water at the stoichiometric composition and stirred for 15 min. A homogeneous slurry was obtained after adding citric acid drop-wise to the solution under continuous stirring for 6 h with molar ratio 1:1 of $(\text{Li}+\text{Ni}+\text{Mn})\text{:C}_6\text{H}_8\text{O}_7$. The pH value was adjusted to 7–8 with ammonium hydroxide. The slurry was transferred into a 100 mL Teflon-lined stainless-steel autoclave maintained at a constant temperature of 180 °C for 12 h. Then the product was dried and calcined at 500 °C for 3 h, and thereafter post-treated at 900 °C for 12 h in air. The AlF_3 -coating layer was fabricated by the chemical deposition method. The as-prepared $\text{Li}_{1.2}\text{Ni}_{0.2}\text{Mn}_{0.6}\text{O}_2$ powders were immersed in the $\text{Al}(\text{NO}_3)_3$ dilute aqueous solution heated to 50 °C and stirred vigorously. NH_4F dilute solution was then added into the solution with the molar ratio of Al to F of 1:3 corresponding to the 5-wt.% AlF_3 coat. After drying at 60 °C in a vacuum oven, the obtained products were heated at 400 °C in ambient argon for 4 h to prevent the formation of Al_2O_3 and secure the formation of AlF_3 -coated $\text{Li}_{1.2}\text{Ni}_{0.2}\text{Mn}_{0.6}\text{O}_2$. Figure 2 displays the pictures of both $\text{Li}_{1.2}\text{Ni}_{0.2}\text{Mn}_{0.6}\text{O}_2$ samples.



Figure 2. Photographs of pristine and AlF_3 -coated $\text{Li}_{1.2}\text{Ni}_{0.2}\text{Mn}_{0.6}\text{O}_2$ specimens.

2.2. Material Characterization

The crystalline phase was identified by XRD using a Philips X'Pert diffractometer (PANalytical, Orsay, France) equipped with $\text{CuK}\alpha$ radiation source ($\lambda = 1.5406 \text{ \AA}$). The diffractograms were recorded at room temperature in the 2θ -range 10–80°. The experimental patterns were refined by the Rietveld method with FULLPROF software program. The variance of the relative amounts of atomic components in the samples were analyzed by inductively coupled plasma-atomic emission spectrometry (ICP-AES, OPTIMA 7000DV, Perkin Elmer Co., Ltd., UK). The morphology and composition were studied by SEM (ZEISS model ULTRA 55) coupled with an energy-dispersive X-ray attached analyzer (EDX). HRTEM images were obtained using an electronic microscope JEOL model JEM-2010. Raman spectra were taken using a micro-Raman spectrophotometer (Horiba, Longjumeau, France) equipped with an optical microscope ($\times 100$ objective) and a 633 nm He–Ne laser excitation line. Data were recorded in steps of 1.6 cm^{-1} with an acquisition time of 30 s. The wavenumber calibration was regularly verified by using the Raman peak at 520 cm^{-1} of a silicon crystal as a reference. BET specific surface area was measured by nitrogen adsorption/desorption at 77 K in a relative pressure $P/P_0 = 0.0$ – 1.0 , with P and P_0 being the equilibrium and saturation pressure, respectively, using a Quantachrome NOVA automated gas sorption analyzer (Anton Paar GmbH, Blankenfelde-Mahlow, Germany). The pore size distribution and pore volume were estimated using the Barrett–Joyner–Halenda (BJH) method [46].

Electrochemical tests were conducted on CR2025-type coin cells assembled in a glove box (moisture and oxygen content $\leq 5 \text{ ppm}$) under argon atmosphere. The procedure to fabricate the

cathode was as follows: 85 wt.% active material, 10 wt.% carbon black as conductive medium, and 5 wt.% polyvinylidene fluoride (PVDF) in N-methyl pyrrolidinone (NMP) solvent were mixed and ground to generate a homogeneous slurry. The slurry was then spread onto an aluminum foil current collector and dried at 80 °C for 2 h to remove the solvent before being pressed. Using such a cathode (loading of $\sim 2 \text{ mg cm}^{-2}$), the electrochemical cells fabricated with lithium sheet as the counter electrode, Celgard 2500 film as the separator filled with $1 \text{ mol L}^{-1} \text{ LiPF}_6$ in a mixture of ethylene carbonate (EC)/dimethyl carbonate (DMC) (1:1) solution (LP30, Merk) as electrolyte. The galvanostatic charge–discharge (GCD) cycles were performed using a potentiostat/galvanostat (workstation VMP3 Bio-Logic, Seyssinet-Pariset, France) in the potential range 2.0–4.8 V. EIS data were collected using a phase sensitive multimeter (model PSM 1700, UK) in the frequency range 0.01 Hz–100 kHz using a voltage bias of 5 mV.

3. Results

3.1. Structure and Composition

The relative concentration of atoms was measured by ICP-AES. Results listed in Table 1 show that the chemical composition of the LLNMO samples is close to the theoretical stoichiometry. Moreover, the amount of Al is consistent with the value expected by the surface treatment. The $\sim 2\%$ loss of Li in pristine LLNMO should be attributed to its departure from the surface during the calcination process. Figure 3 displays the Rietveld refinement of the XRD patterns of pristine and AlF_3 -coated $\text{Li}_{1.2}\text{Ni}_{0.2}\text{Mn}_{0.6}\text{O}_2$ oxides. For both samples, these results suggest the structural co-existence of the Li_2MnO_3 ($C2/m$ S.G.) and $\text{LiNi}_{0.5}\text{Mn}_{0.5}\text{O}_2$ ($R\bar{3}m$ S.G.) phases. XRD diagrams exhibit the typical diffraction patterns of the $\alpha\text{-NaFeO}_2$ -type layered structure with the $R\bar{3}m$ space group (hexagonal setting) [47]. Additional reflections appeared in the $20\text{--}21^\circ$ 2θ -region that are the fingerprints of the Li_2MnO_3 -type $C2/m$ phase. Such a superstructure suggests the presence of Li^+ ions in the transition-metal layer of $\text{Li}_{1.2}\text{Ni}_{0.2}\text{Mn}_{0.6}\text{O}_2$. The existence of this secondary phase is also detected by Raman spectroscopy, as it will be evidenced in the following. For the coated sample, the XRD features are unchanged in agreement with other works [48,49].

Table 1. Elemental composition of LLNMO samples analyzed by ICP-AES.

Sample	Li	Ni	Mn	Al
Pristine	1.18	0.21	0.59	-
AlF_3 -coated	1.20	0.19	0.61	0.048

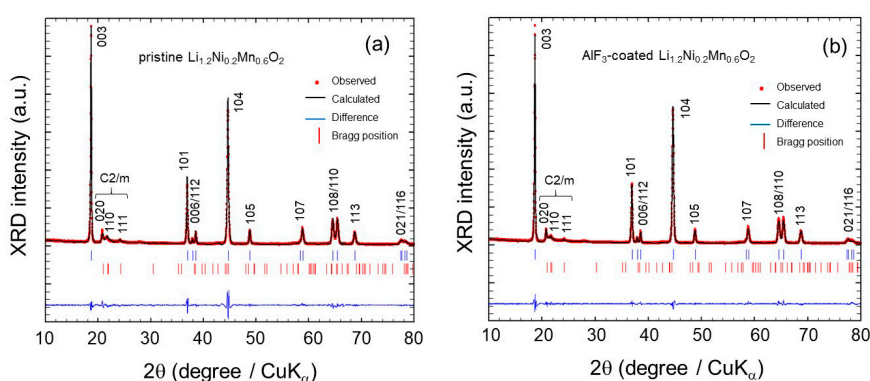


Figure 3. Rietveld refinements for (a) pristine and (b) AlF_3 -coated $\text{Li}_{1.2}\text{Ni}_{0.2}\text{Mn}_{0.6}\text{O}_2$ Li-rich oxides. XRD patterns were recorded using a $\text{CuK}\alpha$ source ($\lambda = 1.5406 \text{ \AA}$).

From the Rietveld refinement results (Table 2), the lattice expansion occurred in both the a and c directions when LLNMO particles are coated with AlF_3 . Thus, the volume of the elementary unit

cell increases slightly with the coating. In stoichiometric $\text{Li}_{1.2}\text{Ni}_{0.2}\text{Mn}_{0.6}\text{O}_2$, the valence state of Mn and Ni ions are +4 and +2, respectively [50,51]. The primary effect of the AlF_3 coating is a reduction of the loss of Li ions at the surface of particles that provokes an increase of the Li_2MnO_3 component content and, consequently, an increase of the amount of Mn^{3+} ions. The slight change of the lattice parameters is explained by consideration of the ionic radii of Mn ions. The increase in a and c is attributable to the bigger ionic radius of Mn^{3+} ions in octahedral coordination (58 pm against 53 pm for Mn^{4+} ions) [52]. It also gives evidence that an internal composite structure exists in the Li-rich oxide framework. This increasing concentration of Mn^{3+} has been reported to be beneficial to the electrochemical performance. The existence of Mn^{3+} causes a gradual activation of Li_2MnO_3 , which results in a capacity increase upon cycling [53]. For the $R\bar{3}m$ phase of $\text{Li}_{1.2}\text{Ni}_{0.2}\text{Mn}_{0.6}\text{O}_2$, the refinement involved fixing the Mn occupancy and varying the ratios of the Ni and Li occupancies on the TM and Li sites. The degree of Ni occupancy in the interlayer Li sites (cationic mixing) is rather low at 1.33% and 1.25% for pristine and coated LLNMO samples, respectively. There are several indicators to evaluate the presence of Li-Ni anti-sites (cation mixing). First, the c/a lattice parameter ratio evidences the deviation of the rock-salt structure (i.e., $c/a > 4.90$). The second indicator is the peak intensity ratio $R_1 = I_{003}/I_{104}$; the higher R_1 , the lower amount of undesirable Li-Ni anti-sites and better hexagonal structure [54]. The third fingerprint of the hexagonal ordering is defined by the factor $R_2 = (I_{006} + I_{102})/I_{101}$; the lower the R_2 , the better the hexagonal ordering [55,56]. The values of R_1 and R_2 reveal that the hydrothermally synthesized LLNMO samples have a perfect layered structure. As seen in Table 2, the Rietveld refinement results are consistent with the direct observation of the XRD peak intensity ratios showing the lower cation mixing with well-ordered rhombohedral structures for the AlF_3 coated LLNMO sample.

Table 2. The structural parameters obtained from Rietveld refinements for pristine and AlF_3 -coated $\text{Li}_{1.2}\text{Ni}_{0.2}\text{Mn}_{0.6}\text{O}_2$ powders prepared by hydrothermal method via citric acid chelator.

Crystal Data	Pristine LLNMO	AlF_3 -Coated LLNMO
a (Å)	2847(3)	2852(1)
c (Å)	14,216(6)	14,235(0)
V (Å ³)	99.82	99.97
c/a	4.992	4991
$I_{(003)}/I_{(104)}$	1.41	1.45
$(I_{(006)} + I_{(102)})/I_{(101)}$	0.42	0.41
Coherent length (L_c) (nm)	68	65
Strain $\times 10^{-2}$	2.45	2.12
Reliability factors		
R_w (%)	6.22	7.55
R_{exp} (%)	4.71	6.23
Ni^{2+} (in Li layer of $R\bar{3}m$)	0.0133	0.0125
Phase fraction (mol %)		
$R\bar{3}m$	48.2	49.5
$C2/m$	51.8	50.5

The local deformation of the crystal structure is investigated by the analysis of the broadening of the XRD reflections according to the Williamson–Hall relationship [57,58]:

$$B \cos\theta = 4 \langle e \rangle \sin\theta + K\lambda/L_c \quad (1)$$

where B is the full-width at half-maximum (FWHM), K is the crystallite shape factor (assumed to be 0.9), $\langle e \rangle$ is the micro-strain field, L_c is the size of the crystallites (coherence length), θ is the diffraction angle and λ is the X-ray wavelength of the source. The microstrain is extracted from the slope of the plot of $B \cos\theta$ vs. $\sin\theta$ in Figure 4, and L_c is determined by extrapolation of the straight line to $\sin\theta = 0$.

Both samples have identical L_c of 65 ± 5 nm. The results show that the microstrain of 2.45×10^{-2} for pristine LLNMO slightly reduces to 2.12×10^{-2} for the coated sample. The smaller value of $\langle \epsilon \rangle$ in the AlF_3 -coated sample proves that the thin layer stabilizes the lattice structure, a consistent result with the fact that the coating process has reduced the number Li-Ni anti-sites by $\sim 7\%$. The decrease of the strain field gives evidence of a better structural stability of the coated sample than the pristine one, as expected from the above discussion devoted to the lattice parameters and the consideration of ionic radii.

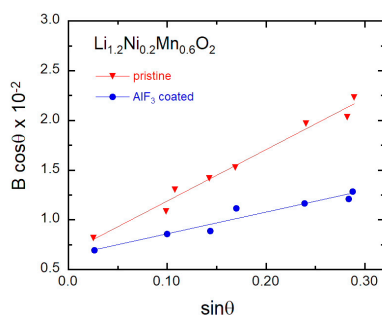


Figure 4. Analysis of the full-width at half-maximum (FWHM) of the XRD reflections according to Equation (1).

The porosity of hydrothermally synthesized LLNMO samples was studied by N_2 adsorption/desorption tests. Figure 5a,b presents the N_2 adsorption/desorption isotherm and the pore-size distribution (inset) for pristine and AlF_3 -coated LLNMO samples. An increase in the amount of adsorbed N_2 with increase of the P/P_0 value and the appearance of a hysteresis loop are observed in the isotherm curves. Results obtained from BJH analysis are listed in Table 3. The average BJH pore width is in the range 4.5–5.5 nm, which indicates that these holes are mainly mesopores with total pore volume of $0.45 \text{ cm}^3 \text{ g}^{-1}$. These features are fingerprints of a hierarchical mesoporous structure of LLNMO powders that promotes the Li^+ ion kinetics [59]. Suib et al. [60] described the formation of mesoporosity by aggregation of nanoparticles along their lateral faces. In the same way, the mesopores (~ 5 nm) correspond here to the voids existing between randomly-packed nanoparticles of ~ 150 nm in diameter inside secondary particles (agglomerates) of ~ 600 nm in size, as we will see on TEM images reported later in this work.

BET analysis shows that pristine and AlF_3 -coated LLNMO samples have a specific surface area of 11.5 and $9.2 \text{ m}^2 \text{ g}^{-1}$, respectively, which is advantageous for enhancing the transport of Li^+ ions in the secondary particles. These values are comparable with those reported by Chang et al. [61] for Li-rich $\text{Li}_{1.27}\text{Cr}_{0.2}\text{Mn}_{0.53}\text{O}_2$ oxides prepared by milling-assisted solid-state process. Xiang et al. [62] reported the influence of polyvinyl alcohol (PVA) as chelating agent on the BET surface area for $\text{Li}_{1.2}\text{Ni}_{0.2}\text{Mn}_{0.6}\text{O}_2$ prepared by sol-gel technique (varying from $\sim 10 \text{ m}^2 \text{ g}^{-1}$ for PVA-0% to $\sim 33 \text{ m}^2 \text{ g}^{-1}$ for PVA-15%). Zhang et al. [63] showed that 3- μm sized secondary particles, which consisted of self-assembled crystallites ~ 150 nm in size, demonstrated optimized mesostructure partially mitigating the voltage fading. The equivalent particle size of the samples can be calculated from the BET data and compare with SEM images. The average particle diameter (in nm) is expressed by the relation [64]:

$$L_{\text{BET}} = \frac{6000}{S_{\text{BET}}d} \quad (2)$$

where S_{BET} is the specific surface area (in $\text{m}^2 \text{ g}^{-1}$) measured by BET experiments and d the gravimetric density (4.53 g cm^{-3} for NMO). The BET surface area and the average particle size results are found in Table 3. We observe a relatively good agreement between particle size values L_{BET} and L_{TEM} evaluated from BET and measured from TEM images, respectively.

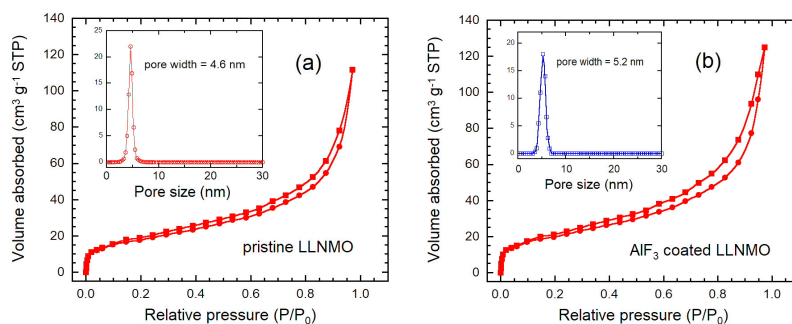


Figure 5. N_2 adsorption-desorption isotherm and Barrett–Joyner–Halenda (BJH) pore-size distribution for (a) pristine and (b) AlF_3 -coated $Li_{1.2}Ni_{0.2}Mn_{0.6}O_2$ oxides.

Table 3. Brunauer–Emmett–Teller (BET) specific surface area, calculated average particle size from BET data (L_{BET}) using Equation (2), mean particle size measured using TEM imaging (L_{TEM}) and results obtained from Barrett–Joyner–Halenda (BJH) analysis for hydrothermally prepared LLNMO samples.

Sample	BET ($m^2 g^{-1}$)	L_{BET} (nm)	L_{TEM} (nm)	Pore Size (nm)	Pore Volume ($cm^3 g^{-1}$)
Pristine	11.5	115	150	4.6	0.45
AlF_3 coated	9.2	144	180	5.2	0.49

The crystal structure of Li-rich layered oxides is currently discussed assuming either the existence of solid solution according to the substitution of M in $LiMO_2$ [65,66] or the formation of a composite of $LiMO_2$ and Li_2MnO_3 [67,68]. The X-ray diffraction analysis clearly pleads for the second model. This hypothesis is also confirmed by Raman spectroscopy, which is efficient in probing the short-range order (local structure) of materials. Regarding the vibrational modes of $Li_{1.2}Ni_{0.2}Mn_{0.6}O_2$ ($0.5Li_2MnO_3 \cdot 0.5LiNi_{0.5}Mn_{0.5}O_2$ in layered notation), two Raman-active modes ($A_{1g} + E_g$) are expected for $LiMO_2$ ($M = Ni$ or Mn , D_{3d}^5 symmetry) [69,70], while six Raman active modes ($4A_g + 2B_g$) are predicted for Li_2MnO_3 (C_{2h}^3 symmetry) [71]. In Figure 6, we observe two peaks at 603 and 482 cm^{-1} , which are assigned to the stretching $\nu(MO_6)$ and bending $\delta(O-M-O)$ vibration with $M = Mn^{4+}$, Ni^{2+} belonging to the $LiNi_{0.5}Mn_{0.5}O_2$ phase and three peaks at 587 , 437 , and 416 cm^{-1} attributed to the Li_2MnO_3 phase. The extra-peak at ca. 650 cm^{-1} is attributed to the stretching vibration $\nu(Mn^{3+}O_6)$. The calculated spectrum is shown in Figure 6 (black line). The Raman spectrum of the surface-modified LLNMO sample does not exhibit any frequency shift with respect to the pristine one. This indicates that the AlF_3 coating does not influence the Li-rich local structure, and that neither Al nor F penetrated into the samples in agreement with the XRD analysis.

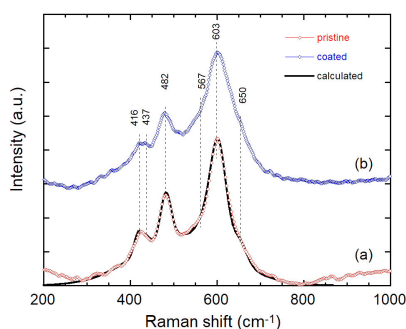


Figure 6. Raman spectra of LLNMO materials recorded with the laser excitation line at 532 nm. The solid black line represents the calculated spectrum.

3.2. Morphology

The morphology of LLNMO powders has been investigated by SEM and HRTEM imaging. Figure 7 presents the SEM images combined with the EDX spectrum of the surface of AlF_3 -coated sample. The SEM images show regular particles with similar morphology (almost monodisperse). The homogeneous size distribution of agglomerates ~ 200 nm is noticeable without difference between pristine and AlF_3 -coated particles. The EDX spectrum (Figure 7c) of the AlF_3 -coated sample exhibits only the additional peak of Al, because the peak of fluorine merges with that of Mn. No other element was detected, giving evidence of the absence of any impurity in all the samples. From this experiment, the concentration of Al is found to be 5.15 wt.%.

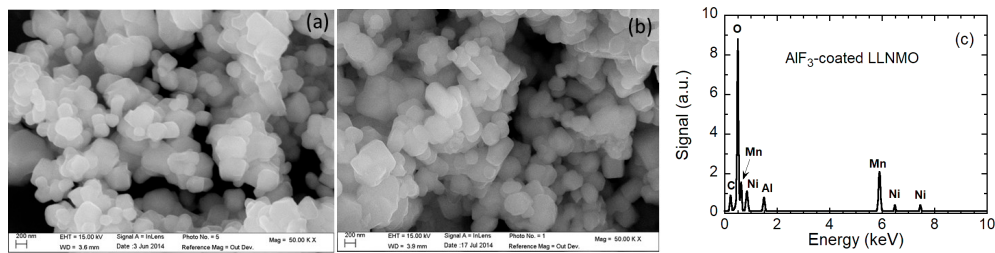


Figure 7. SEM images of (a) pristine LLNMO and (b) AlF_3 -coated LLNMO. (c) EDX spectrum of AlF_3 -coated LLNMO.

The HRTEM images for all the samples are reported in Figure 8. The 200 nm-thick agglomerates of the $\text{Li}_{1.2}\text{Ni}_{0.2}\text{Mn}_{0.6}\text{O}_2$ samples are made of well-crystallized particles 95 nm in size. The comparison between HRTEM images shows that the coating had no effect on the size of particles. There is no effect on the shape, confirming that the coating of only 5–7 nm thickness does not change the structure nor the morphology of the powders [72,73]. This is due to the relatively low temperature of 400 °C used during the coating process, which is much smaller than the temperature at which the particles could start to coalesce. The distance between neighboring fringes shown in insets is 0.47 nm, which is assigned to (003), (001), or both planes for rhombohedral, monoclinic, or both phases, respectively. Such features are commonly observed in Li-rich samples of different compositions [74].

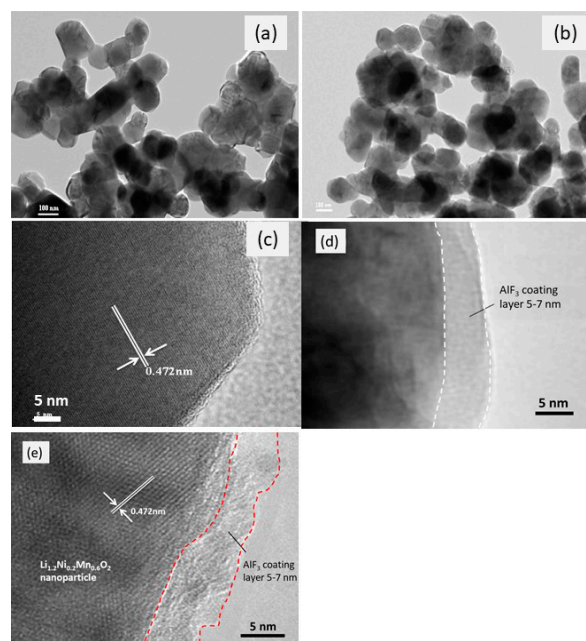


Figure 8. TEM images of (a) pristine LLNMO and (b) AlF_3 -coated LLNMO. HRTEM images of (c) pristine LLNMO and (d) AlF_3 -coated LLNMO. Image (e) shows the morphology of the AlF_3 coating.

3.3. Electrochemical Properties

Electrochemical properties of LLNMO samples have been investigated by galvanostatic charge-discharge and electrochemical impedance spectroscopy. In this study, we consider the total charge delivered by each component of the LLNMO cathodes ($x\text{Li}_2\text{MnO}_3 \cdot (1-x)\text{LiNi}_{0.5}\text{Mn}_{0.5}\text{O}_2$). As $x = 0.5$ for $\text{Li}_{1.2}\text{Ni}_{0.2}\text{Mn}_{0.6}\text{O}_2$, the theoretical specific capacity is 369 mAh g^{-1} (229 mAh g^{-1} for $0.5\text{Li}_2\text{MnO}_3 + 140 \text{ mAh g}^{-1}$ for $0.5\text{LiNi}_{0.5}\text{Mn}_{0.5}\text{O}_2$). This value is exactly the theoretical capacity, based on complete extraction of lithium (1.2 Li per $\text{Li}_{1.2}\text{Ni}_{0.2}\text{Mn}_{0.6}\text{O}_2$ formula unit) [75–77]. The theoretical discharge capacity, based on the mass of the discharged rock-salt product after the first charge/discharge cycle, is 280 mAh g^{-1} . Note that for unknown reasons, some authors used the value of 200 mAh g^{-1} . For clarity, we use the current density expressed in mA g^{-1} with the correspondence $1\text{C} = 369 \text{ mA g}^{-1}$ for all the electrodes.

Figure 9a,b display the GCD curves of pristine and AlF_3 -coated $\text{Li}_{1.2}\text{Ni}_{0.2}\text{Mn}_{0.6}\text{O}_2$ electrodes, respectively, performed at 0.15C rate in the potential window $2.0\text{--}4.8 \text{ V}$. The shape and change after the first activation cycle are consistent with literature [9,41,44,50,78–82]. The initial charge occurred with a well-defined voltage plateau at 4.5 V , which correspond to the irreversible extraction of Li_2O from the Li_2MnO_3 component [8]. Thus, the strong oxidation of O^{2-} is considered to occur at ca. 4.5 V . The capacity corresponding to the oxidation of Ni from Ni^{2+} to Ni^{4+} (below 4.5 V) is ca. 100 mAh g^{-1} for both electrodes. During the initial discharge, the pristine and coated LLNMO electrodes delivered a specific capacity of 242 and 260 mAh g^{-1} , respectively, which was maintained at 219 and 231 mAh g^{-1} after 50 cycles. After 100 cycles of charge-discharge at 600 mA g^{-1} current density, the capacity retention of $\sim 91\%$ for the coated electrode is higher than that of pristine LLNMO ($\sim 59\%$).

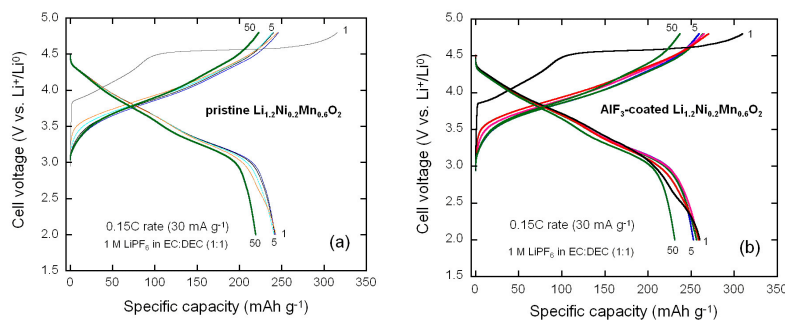


Figure 9. Galvanostatic charge-discharge of (a) pristine LLNMO and (b) AlF_3 -coated LLNMO. Cycles were carried out at 30 mA g^{-1} current density (0.08C rate) in the potential range $2.0\text{--}4.8 \text{ V}$.

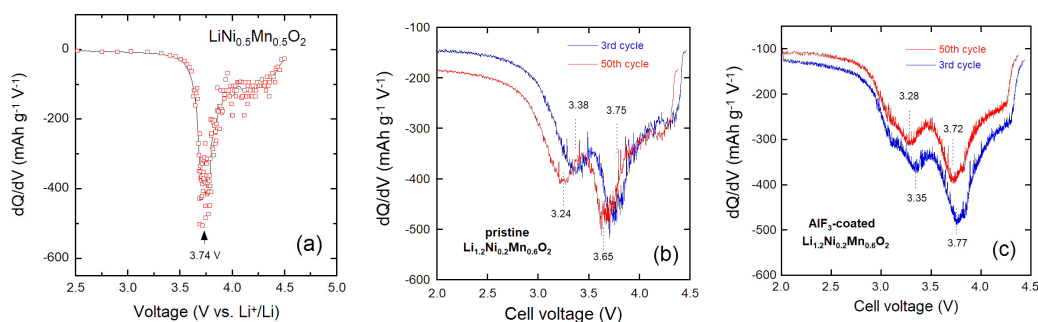


Figure 10. Incremental capacity ($-\text{d}Q/\text{d}V$ vs. V) plots for (a) $\text{LiNi}_{0.5}\text{Mn}_{0.5}\text{O}_2$, (b) pristine LLNMO, and (c) AlF_3 -coated LLNMO.

Figure 10a–c present the differential capacity or incremental capacity (IC) plots ($-\text{d}Q/\text{d}V$ vs. V) for discharge curves of LLNMO electrodes at the 3rd and 50th cycles, which not only specify the reduction potentials but also clearly display the voltage fade issue. In IC plots, the peaks correspond to the

pseudo plateaus in the GCD curves. The IC curve of the parent $\text{LiNi}_{0.5}\text{Mn}_{0.5}\text{O}_2$ (Figure 10a) confirms that the peak at ca. 3.74 V is due to the reduction of Ni^{4+} to Ni^{3+} during the insertion of Li^+ ions in the layered framework. This reduction peak (A) occurred at 3.75 and 3.77 V in the discharge profile of pristine and coated electrodes, respectively. It is shifted down to ~ 3.65 V after 50 cycles for pristine $\text{Li}_{1.2}\text{Ni}_{0.2}\text{Mn}_{0.6}\text{O}_2$, whereas a shift by only 70 mV is observed for the AlF_3 -coated electrode. The main difference between $\text{LiNi}_{0.5}\text{Mn}_{0.5}\text{O}_2$ and $\text{Li}_{1.2}\text{Ni}_{0.2}\text{Mn}_{0.6}\text{O}_2$ is the occurrence of the low-voltage cathodic peak (B) at ca. 3.25–3.35 V, which is assigned to the reduction of Mn^{4+} to Mn^{3+} in MnO_2 formed during the first charging reaction [38,59,83]. Note that the reduction peak of Mn^{4+} is weaker for AlF_3 -coated $\text{Li}_{1.2}\text{Ni}_{0.2}\text{Mn}_{0.6}\text{O}_2$ than $\text{Li}_{1.2}\text{Ni}_{0.2}\text{Mn}_{0.6}\text{O}_2$; however, the voltage decay of the B peak is higher than that of the A peak.

Figure 11 presents the rate capability and the cycling stability of LLNMO electrodes synthesized by the hydrothermal method assisted with citric acid. Experiments were carried out in the voltage range 2.0–4.8 V at various current densities in the range 30–900 mA g^{-1} . As shown in Figure 11a, specific capacities of 116 and 153 mAh g^{-1} are obtained at the 900 mA g^{-1} rate during the discharge process of pristine and AlF_3 -coated electrodes, respectively. The decay in the specific capacity was observed without significant change in the S-shape of the charge and discharge curves. From the cycling performance shown in Figure 11b, the loss of capacity calculated upon 100 cycles is found to be 0.75 and 0.20 mAh g^{-1} per cycle for the pristine and AlF_3 -coated electrodes, respectively. The good reversibility of the AlF_3 -coated $\text{Li}_{1.2}\text{Ni}_{0.2}\text{Mn}_{0.6}\text{O}_2$ electrode is confirmed by the Coulombic efficiency remaining around 99.4% over 100 cycles (Figure 11b). The rates of capacity fade for the AlF_3 -coated electrode are 0.29 and 0.41 mAh g^{-1} per cycle, when tested over 80 cycles at current densities of 300 and 900 mA g^{-1} , respectively (Figure 11c). The evolution of the Coulombic efficiency for pristine and AlF_3 -coated LLNMO electrodes is presented in Figure 11d. In comparison, the Coulombic efficiency of 76% for pristine LLNMO in the first cycle has increased to 87% after AlF_3 coating. Similar behavior was reported by Liu et al. [43] for ZnAl_2O_4 -coated $\text{Li}_{1.2}\text{Ni}_{0.2}\text{Mn}_{0.6}\text{O}_2$ material.

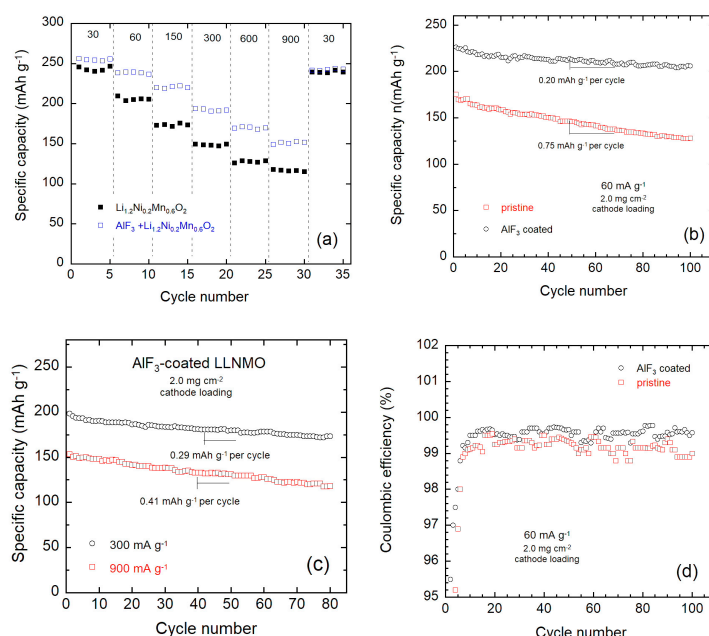


Figure 11. (a) Rate performance (current densities in mA g^{-1}) and (b) cycling stability of pristine and AlF_3 -coated LLNMO electrodes tested at current density of 30 mA g^{-1} . (c) Cyclability of the AlF_3 -coated LLNMO electrode tested at current density of 300 and 900 mA g^{-1} . (d) Coulombic efficiency of pristine and AlF_3 -coated LLNMO electrodes.

The present electrochemical performances of LLNMO electrodes are comparable with previous data. However, there are some differences depending on the morphology of the active particles.

Hydrothermally synthesized rod-like hierarchical nano/micro $\text{Li}_{1.2}\text{Ni}_{0.2}\text{Mn}_{0.6}\text{O}_2$ delivered a capacity of 212 mAh g^{-1} after 30 cycles at 1C rate (250 mA g^{-1}) [36]. Yang et al. [32] reported a specific capacity of $\sim 190 \text{ mAh g}^{-1}$ at 1C rate (250 mA g^{-1}) for agglomerated $\text{Li}_{1.2}\text{Ni}_{0.2}\text{Mn}_{0.6}\text{O}_2$ particles with a large pore volume of $9.2 \times 10^{-3} \text{ cm}^3 \text{ g}^{-1}$ prepared by sol-freeze-drying method. $\text{Li}_{1.2}\text{Ni}_{0.2}\text{Mn}_{0.6}\text{O}_2$ nanoparticles (100–200 nm in size) coated with a thin layer of Li^+ -conductive Li_2ZrO_3 coating obtained through a synchronous lithiation strategy delivered a capacity of circa 169 mAh g^{-1} over 100 cycles at current density 200 mA g^{-1} [13].

To further investigate the effect of the AlF_3 coating on resistances and lithium kinetics in LLNMO, EIS measurements were carried out. Figure 12 presents the EIS spectra investigated after the first cycle performed at 0.15C rate. As shown in Figure 12a, all of the Nyquist plots of the cells are composed of three contributions that can be modeled using the equivalent circuit shown as inset: (i) the intercept of x -axis at high-frequency corresponds to the ohmic resistance (R_s), i.e., electrodes and electrolyte contributions; (ii) a depressed semicircle in the high-frequency region is ascribed to the charge transfer impedance (R_{ct} , CPE_{ct}) at the electrode/electrolyte interface, in which the constant phase element is expressed by $\text{CPE} = 1/T((j\omega)^p)$ with ω the angular frequency, T a CPE constant and p an exponent ($0 \leq p \leq 1$, $p = 1$ for pure capacitance) and j is the imaginary number ($j = \sqrt{-1}$); and finally (iii) an inclined line (with a slope of $\sim 45^\circ$) at low-frequency reflects the diffusion-controlled process characterized by a Warburg impedance taken in the infinite limit and expressed by the relation $Z_W(\omega) = \sigma_w (1 - j) \omega^{-1/2}$, where σ_w is the Warburg factor [84]. The real part of the impedance $Z'(\omega)$ is the sum of the components:

$$Z'(\omega) = R_s + R_{ct} + R_{SEI} + \sigma_w \omega^{-1/2} \quad (3)$$

From the slope of the Z' vs. $\omega^{-1/2}$ curves (Figure 12b), we can calculate the apparent chemical diffusion coefficient of Li^+ ions (D_{Li^+}) in the electrode using the relation [85]:

$$D_{\text{Li}^+} = \frac{1}{2} \left[\frac{RT}{F^2 A C_{\text{Li}} \sigma_w} \right]^2 \quad (4)$$

where R is the gas constant, F is Faraday's constant, T the absolute temperature, A the surface area of the electrode-electrolyte interface, and C_{Li} the molar concentration of Li^+ ions in the electrode (0.8 mmol cm^{-3}). The fitting parameters are reported in Table 4. Results can be summarized as follows. The value of R_{ct} for the cell with AlF_3 -coated $\text{Li}_{1.2}\text{Ni}_{0.2}\text{Mn}_{0.6}\text{O}_2$ (65.5Ω) is smaller than that of pristine $\text{Li}_{1.2}\text{Ni}_{0.2}\text{Mn}_{0.6}\text{O}_2$ (100.3Ω), demonstrating that the AlF_3 coating layer effectively decreases the interface contact resistance. In addition, the exponent p of the CPE component associated with the charge transfer is close to unity for both cells, which means that the CPE contribution is essentially capacitive. This gives evidence of a good homogeneity of the electrode. Note that the contribution of the SEI layer can be neglected. As a result, the apparent diffusion coefficients of Li^+ ions are found to be 2.8×10^{-15} and $1.1 \times 10^{-14} \text{ cm}^2 \text{ s}^{-1}$ in pristine and AlF_3 -coated $\text{Li}_{1.2}\text{Ni}_{0.2}\text{Mn}_{0.6}\text{O}_2$ electrodes, respectively.

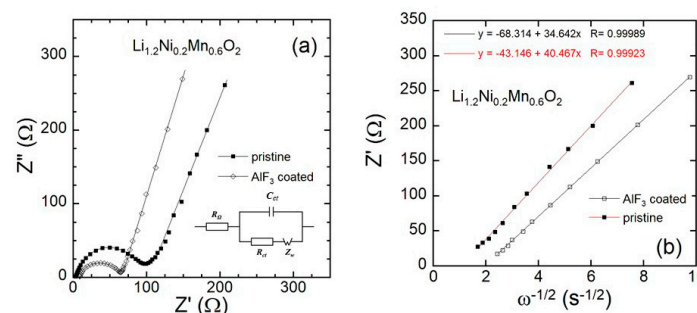


Figure 12. (a) Nyquist plots of the cell with pristine and AlF_3 -coated $\text{Li}_{1.2}\text{Ni}_{0.2}\text{Mn}_{0.6}\text{O}_2$ cathodes. (b) plots of Z' vs. $\omega^{-1/2}$. Solid lines are the fits using the equivalent circuit shown as inset.

The D_{Li} + calculated values of our hydrothermally synthesized LLNMO samples are slightly higher than the values reported from Yang et al. [39] and Lin et al. [44]. D_{Li} + of 2.34×10^{-17} and $1.03 \times 10^{-14} \text{ cm}^2 \text{ s}^{-1}$ was reported for pristine LLNMO and LLNMO/graphene structures synthesized by sonication in ethylene glycol solution [39]. D_{Li} + measured for LLNMO prepared by a sol-gel method assisted with carbon felt as reactive carrier was $2.49 \times 10^{-16} \text{ cm}^2 \text{ s}^{-1}$ before charging, which is slightly smaller than $4.71 \times 10^{-16} \text{ cm}^2 \text{ s}^{-1}$ obtained under charge at 4.8 V [44]. In contrast, Sasakawa et al. [86] reported a higher D_{Li} + value of $1.6 \times 10^{-13} \text{ cm}^2 \text{ s}^{-1}$ in the discharge state of LLNMO particles prepared by combustion method. The same group of researchers showed that D_{Li} increased with increasing the charge rate in the potential range 2.5–4.4 V with an average value of $4.5 \times 10^{-13} \text{ cm}^2 \text{ s}^{-1}$ at mid-voltage.

Table 4. Transport parameters of $\text{Li}_{1.2}\text{Ni}_{0.2}\text{Mn}_{0.6}\text{O}_2$ electrodes deduced from EIS measurements.

Sample	R_s (Ω)	R_{ct} (Ω)	CPE _{ct}		σ_w ($\Omega \text{ s}^{-1/2}$)	D_{Li} ($\text{cm}^2 \text{ s}^{-1}$)
			T	p		
pristine	8.4	100.3	2.6×10^{-5}	0.91	40.5	2.8×10^{-15}
AlF ₃ coated	9.1	65.5	4.8×10^{-6}	0.94	34.6	1.1×10^{-14}

Generally, a high D_{Li} + value implies a well-ordered layer structure of the cathode material and a minimum cationic disorder in the Li slabs [87]. Such an Li^+ diffusion enhancement is attributed to the presence of the thin AlF₃ layer, which promotes the ionic transport at the electrode-electrolyte interface and partly suppresses the spinel layer formation. Liu et al. [29] reported D_{Li} values of 8.2×10^{-13} and $3.8 \times 10^{-12} \text{ cm}^2 \text{ s}^{-1}$ for pristine and $\text{Li}_{1.3}\text{Al}_{0.3}\text{Ti}_{1.7}(\text{PO}_4)_3$ (LATP) coated $\text{Li}_{1.2}\text{Ni}_{0.2}\text{Mn}_{0.6}\text{O}_2$, respectively. The samples were synthesized by co-precipitation with the LATP layer ~4 nm thick and exhibited a cationic mixing of 2%. Liu et al. [43] estimated D_{Li} values of 8.2×10^{-14} and $7.6 \times 10^{-12} \text{ cm}^2 \text{ s}^{-1}$ at mid-voltage (3.5 V) for pristine and $\text{Li}_{1.2}\text{Ni}_{0.2}\text{Mn}_{0.6}\text{O}_2$ coated with 1 wt.% ZnAl_2O_4 . Recently, Ku et al. [88] proposed a new Li diffusion model based on the correlation between asymmetric TM migration and Li mobility that explained the non-equivalent intercalation and de-intercalation kinetics. Chang et al. [61] suggested that the high Li-ion diffusion coefficient of $3.9 \times 10^{-10} \text{ cm}^2 \text{ s}^{-1}$ in Li-rich layered cathode material is caused by the mesoporous network composed of tiny primary particles.

To further verify the improvement of the electrochemical properties of the electrodes, EIS measurements were conducted at different discharge cycles. Figure 13a,b presents the variation of the transport parameters R_s , R_{ct} , and σ_w for both LLNMO samples. Among those parameters listed, R_{ct} is the most important since it represents the charge transfer within the cathode material. After 50 charge-discharge cycles, R_{ct} increased by a factor of 2 for both electrodes but seems to saturate at ca. 145 Ω for the AlF₃-coated LLNMO material. These results show that σ_w for pristine LLNMO increases almost linearly upon cycling, while it reaches a value of 50 $\Omega \text{ s}^{-1/2}$ for the AlF₃ coated electrode after 30 cycles.

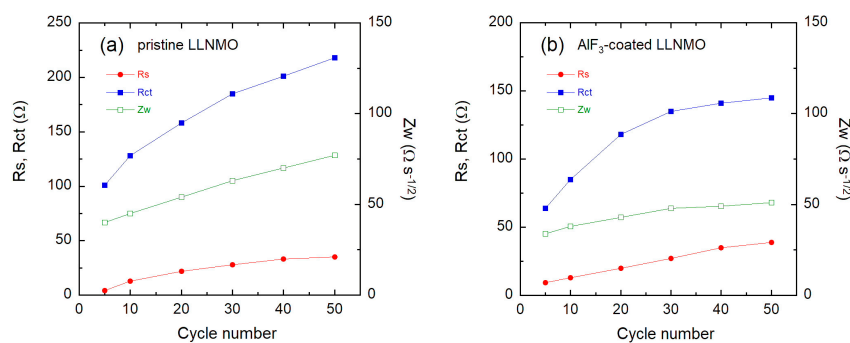


Figure 13. Evolution of the transport parameters R_s , R_{ct} , and σ_w as a function of cycling for (a) pristine and (b) AlF₃-coated LLNMO samples.

Raman spectroscopy is a non-destructive and sensitive method to perform post-mortem studies of cycled cathode materials [89]. This analytical technique allows the investigations of structural changes at the particle surface, the electrode degradation, and the formation of spinel-like layer [28,80,83,90]. In which case, such surface modifications are not detected by diffraction techniques. Figure 14 shows the ex situ Raman spectra of cycled pristine and AlF₃-coated LLNMO electrodes after 50 and 100 cycles. The formation of the spinel-like layer in all cycled LLNMO electrodes is indicated by the shoulder at ~650 cm⁻¹. After long-term cycling (100 cycles) of the pristine LLNMO sample, the intensity of this spectral feature becomes relatively strong, revealing the formation of a disorder on the particle surface. Simultaneously, a broadening and a frequency shift of the peak at 416 cm⁻¹, related to the monoclinic Li₂MnO₃ phase, are observed. In contrast, the AlF₃-coating retards the transformation to the spinel structure of the Li_{1.2}Ni_{0.2}Mn_{0.6}O₂ cathode surface. These studies confirm that the AlF₃ coating is a very efficient surface modification to improve the stability of the layered phase of the Li-rich material, at the origin of the significant improvement of the electrochemical properties.

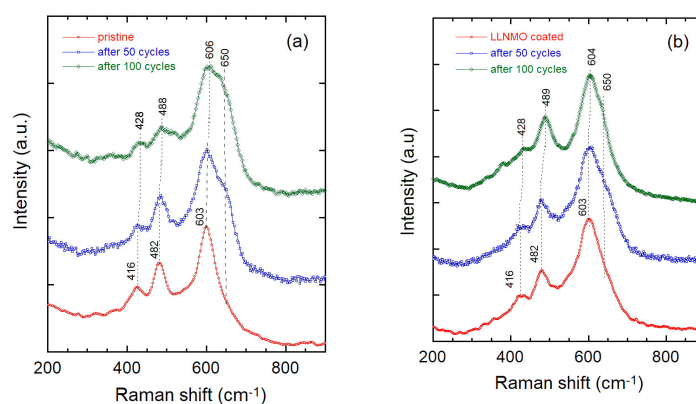


Figure 14. Ex situ Raman spectra of (a) pristine and (b) AlF₃-coated LLNMO electrodes after 50 and 100 cycles at 30 mA g⁻¹ current density.

4. Discussion

4.1. Structural Stability

The structural and electrochemical stability of LLNMO strongly depend on synthesis conditions and operating parameters. The stable performance in relation to initial charge condition shows that a fast rate of 3C induced a decrease of the R_{ct} resistance and slight increase of the Li⁺ diffusion coefficient in the bulk. Our results confirm the efficiency of the AlF₃ coating with the optimized concentration of 5 wt.% [86]. This layer is thick enough to protect the electrode material against the side reactions with the electrolyte, which reduces the resistance of the SEI layer, and increases the rate capability. The coating layer also stabilizes the layered network, with two beneficial effects: (i) it increases the cycle ability, which improves the cycle ability and (ii) it increases the diffusivity of Li⁺, which contributes to enhancing the rate capability of the coated particles. In addition, the mesopores increase the effective surface area in contact with the electrolyte, which explains the high capacities reported in this work.

Improvement of calendar and cycling life together with safety issues of lithium-ion batteries require sophisticated technology to prevent degradation mechanisms. The surface modification of the electrode materials is part of the solution [91]. Among the unwanted degradation mechanisms occurring in LLNMOs, the creation of the solid electrolyte interphase (SEI), growth of a layered-to-spinel surface layer, unreacted residual lithium ingredients on the particle surface, formation of corrosion pits, and occurrence of inter-granular cracks inside primary particles have been widely documented [92–98].

To date, few works report the use of AlF₃ as a deposit on the surface of Li-rich Mn-rich particles [48,71,98–100]. Sun et al. [71] consider the AlF₃ coating layer as a “buffer” through which the activity of extracted oxygen is reduced; thus, the electrolyte decomposition is avoided at voltages above

4.5 V. AlF_3 is preferable to Al_2O_3 , which is unstable in Li cells and can be peeled off from the cathode surface by conversion into AlF_3 in the presence of traces of HF in the electrolyte. AlF_3 is also preferable to Li_3PO_4 . Kang and Thackeray reported a surface coating of Li-Ni-PO_4 , leading to reversible capacity of 200 mAh g^{-1} at 1C. They speculated that one of the components Li_3PO_4 acts as an excellent lithium ion conductor as well as an efficient protective layer stabilizing the electrode surface, though it is not clear how Li_3PO_4 stabilizes the electrode surface [101]. Then, Liu et al. used this coating to stabilize the interface and reduce the side reaction between the material and electrolyte and thus improve the cyclic stability of a Li-rich, Mn-containing layered material [101]. Lee et al. [102] synthesized a Li_3PO_4 -coated $\text{Li}_{1.2}\text{Mn}_{0.6}\text{Ni}_{0.2}\text{O}_2$, which delivered 240 mAh g^{-1} at 0.1C (25 mA g^{-1}), and 205 mAh g^{-1} after 50 cycles at room temperature, which corresponds to 85% capacity retention over 50 cycles, compared to ~91% capacity retention after 100 cycles at 2C in our AlF_3 -coated $\text{Li}_{1.2}\text{Ni}_{0.2}\text{Mn}_{0.6}\text{O}_2$ electrode. More recently, $\text{Li-rich@Li}_3\text{PO}_4$ was synthesized via a template of polydopamine [103]. The nanoparticles were 100–200 nm thick, comparable to the particles in the present work (secondary particles 200 nm, primary particles 95 nm). The beneficial protection effects against side-reactions with the electrolyte were confirmed. Actually, almost all coatings that are chemically and electrochemically stable with the carbonate electrolytes (including Li_3PO_4 and AlF_3) have this function (see [104] for a review). However, the results were not competitive with the results obtained with other coatings such as AlF_3 . For instance, at 0.2C ($1\text{C} = 200 \text{ mA g}^{-1}$) in a potential window from 2.0 to 4.8 V (the same conditions as in the present work), $\text{Li-rich@Li}_3\text{PO}_4$ delivered a capacity of 230 mAh g^{-1} , which decreased to 130 mAh g^{-1} after 100 cycles. Therefore, the Li_3PO_4 coat fails to reduce the kinetics of the phase transition to the spinel phase or Mn dissolution in the surface layer of $\text{Li}_{1.2}\text{Ni}_{0.2}\text{Mn}_{0.6}\text{O}_2$, while it was found efficient in the case of NMC ($\text{Li}(\text{Ni}_{1/3}\text{Mn}_{1/3}\text{Co}_{1/3})\text{O}_2$ and $\text{Li}(\text{Ni}_{0.5}\text{Mn}_{0.3}\text{Co}_{0.2})\text{O}_2$), where it prevents NiO-like and Co-like phase formations on the surface [105,106]. Zheng et al. [98] analyzed the fundamental functions of the AlF_3 coating and concluded that the coating mitigates the acidic attack by the electrolyte of spinel-like networks formed on the particle surface. Figure 15 illustrates the transformation mechanism of an active particle of Li-rich layered oxide. Upon repeated cycling, the morphology of the uncoated particle is modified with the formation a spinel phase and corrosion pits, whereas a thin layer of coating protects the particles against corrosion and postpones the spinel growth. The efficiency of the AlF_3 coating is also evidenced by the fact that our results were obtained with only 5-wt.% AlF_3 , while effective protection of cathode elements often need much thicker coats; for instance, 12 wt.% in the case of $\text{LiAlO}_2/\text{Al}_2\text{O}_3$ -coated nano- LiCoO_2 [107].

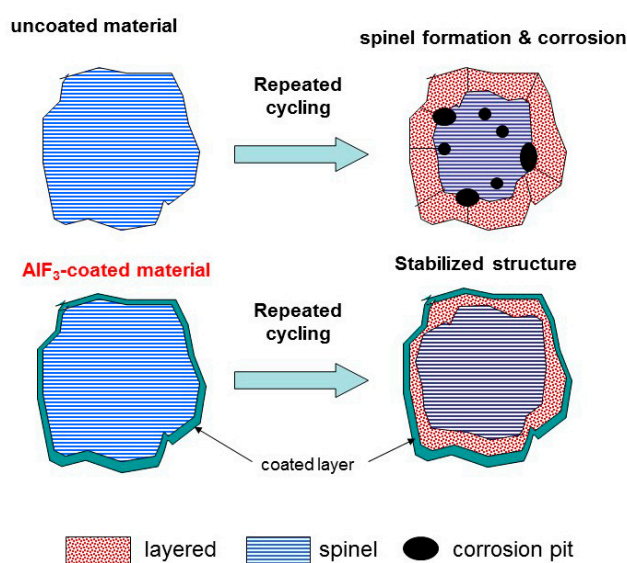


Figure 15. Scheme of transformation of active particle of Li-rich layered oxide upon repeated cycling. Reproduced with permission from [97]. Copyright 2014, American Chemical Society.

4.2. Voltage Decay

Capacity fading and voltage decay are the important drawbacks of Li-rich cathode materials; they are the main challenges for the commercialization of LLNMOs. The voltage decay originates from a gradual phase transformation of the layered phase to a 3 V spinel-like phase. [13,76,108–113]. From GCD curves and dQ/dV plots, Lee and Manthiram showed that the length of the plateau region during first charge is the primary governing factor in the voltage decay process [111]. From first principles calculations, Xu et al. [112] have suggested that both the formation of $\text{Li}_{\text{tet}}\text{-V(TM)Li-Li}_{\text{tet}}$ dumbbell structures (Li_{tet} refers to the lithium ion in a tetrahedral site and V(TM)Li refers to the lithium-ion vacancy in the TM layer) and TM ion migration into the lithium layer can facilitate the formation of a 3 V spinel-like phase during charging in the high voltage region. The formation of such $\text{Li}_{\text{tet}}\text{-V(TM)Li-Li}_{\text{tet}}$ dumbbell structures can be expected to increase with the length of the plateau region during the first charge process since lithium ions from the TM layer will be extracted once all of the lithium ions are extracted from the lithium layer.

From IC plots (Figure 10) the voltage decay is found to be 2.80 and 1.40 mV per cycle for pristine and AlF_3 -coated electrode, respectively, after 50 cycles. Table 5 lists the voltage decay rate for $\text{Li}_{1.2}\text{Ni}_{0.2}\text{Mn}_{0.6}\text{O}_2$ cathode materials synthesized by different methods. Li et al. [76] inhibited the undesired layered-spinel intergrowth by doping with K^+ ions, which weakened the creation of tri-vacancies in the Li layer and Mn migration. Chong et al. [112] fabricated a spherical core-shell structure, $\text{Li}_{1.2}\text{Ni}_{0.2}\text{Mn}_{0.6}\text{O}_2@ \text{Li}_{1.2}\text{Ni}_{0.4}\text{Mn}_{0.4}\text{O}_2$ by in situ hydrothermal technique, which exhibited a high voltage retention value of 3.335 V after 100 cycles. The most impressive low voltage decay rate of 1.09 mV per cycle was recently reported by Ding et al. [113] for $\text{Li}_{1.2}\text{Mn}_{0.6}\text{Ni}_{0.2}\text{O}_2$ microspheres. The sophisticated modification made by a three-in-one surface treatment consisted of synchronous design of oxygen vacancies, spinel-phase integration, and N-doped carbon monolayers.

Table 5. Voltage decay rate for different Li-rich $\text{Li}_{1.2}\text{Ni}_{0.2}\text{Mn}_{0.6}\text{O}_2$ cathode materials.

Material	ΔV per Cycle (mV)	Measurement Conditions	Ref.
Al^{3+} doping	3.50	2.0–4.8 V, 100 cycles @ 25 mA g^{-1}	[26]
Nb^{5+} doping	2.61	2.0–4.8 V, 100 cycles @ 0.1C	[114]
pristine (sol-gel)	1.07	2.0–4.75 V, 200 cycles @ 0.2C	[11]
pristine (co-precipitation)	1.25	2.0–4.75 V, 200 cycles @ 0.2C	[11]
pristine (hydrothermal)	0.75	2.0–4.75 V, 200 cycles @ 0.2C	[11]
Li_2ZrO_3 coating	1.25	2.5–4.5 V, 100 cycles @ 1C	[13]
$\text{Li}_{1.3}\text{Al}_{0.3}\text{Ti}_{1.7}(\text{PO}_4)_3$ coating	4.68	2.0–4.75 V, 80 cycles @ 0.2C	[29]
pristine (co-precipitation)	6.42	2.0–4.8 V, 100 cycles @ 0.2C	[14]
LiAlO_2 coating	3.31	2.0–4.8 V, 100 cycles @ 0.2C	[14]
pristine (co-precipitation)	7.16	2.0–4.75 V, 50 cycles @ 0.2C	[43]
ZnAl_2O_4 coating	5.26	2.0–4.75 V, 50 cycles @ 0.2C	[43]
N-doped carbon coating	1.09	500 cycles @ 5C	[115]
pristine (hydrothermal)	2.80	2.0–4.8 V, 50 cycles @ 0.1C	this work
AlF_3 coating	1.40	2.0–4.8 V, 50 cycles @ 0.1C	this work

The remarkable results by Zheng et al. deserve to be cited [11]. The voltage fade was mitigated by improving the atomic level uniformity of elemental distribution at the $\text{Li}_{1.2}\text{Ni}_{0.2}\text{Mn}_{0.6}\text{O}_2$ surface. Studies of the influence of the synthesis methods (i.e., sol-gel (SG), co-precipitation (CP), and hydrothermal (HT)) on the voltage-decay rate were carried out using secondary ion mass spectroscopy (SIMS), and it was suggested that one of the main reasons for the high voltage-decay rate in HT samples is the non-uniform distribution of Ni ions with a Ni-rich particle surface leading to an easy reduction of the Mn^{4+} ions. Ni-segregated materials also exhibit poor cycling stability.

5. Conclusions

In summary, this work has shown that significant improvements of the electrochemical performance of $\text{Li}_{1.2}\text{Ni}_{0.2}\text{Mn}_{0.6}\text{O}_2$ electrode materials synthesized by hydrothermal technique have been obtained by an optimized AlF_3 coating layer (5 wt.%) deposited on the surface of the 200-nm thick particles. This coating improved all aspects of the electrochemical properties: discharge capacity, capacity retention (~91% over 100 cycles for the coated electrode in contrast with ~59% for the pristine one), and rate capability. The mesoporous morphology of hydrothermally synthesized $\text{Li}_{1.2}\text{Ni}_{0.2}\text{Mn}_{0.6}\text{O}_2$ electrode materials contributed to enhancing the capacity. Another advantage of the AlF_3 coating is the smaller loss of the operating voltage, half that of the pristine sample. Finally, despite certain claims in the literature, these studies have demonstrated the effectiveness of this coating in terms of structural stability, migration of Mn^{3+} cations, attenuation of cross growth in the spinel phase, and protection against side reactions with the electrolyte. Note the results have been obtained by coating pristine $\text{Li}_{1.2}\text{Ni}_{0.2}\text{Mn}_{0.6}\text{O}_2$. The next step should then be to coat doped- $\text{Li}_{1.2}\text{Ni}_{0.2}\text{Mn}_{0.6}\text{O}_2$ using the doping processes mentioned in the introduction, which improved the rate capability by increasing the diffusion coefficient of Li^+ ions in the structure and mitigated the oxidation of O^{2-} ions, in order to benefit from the synergetic effects.

Author Contributions: Conceptualization, C.M.J.; methodology, A.A.-G. and A.M.H.; writing—review and editing, A.M.; supervision, C.M.J. All authors have read and agreed to the published version of the manuscript.

Funding: This research received no external funding.

Conflicts of Interest: The authors declare no conflict of interest.

References

1. Zaghib, K.; Mauger, A.; Groult, H.; Goodenough, J.B.; Julien, C.M. Advanced electrodes for high power Li-ion batteries. *Materials* **2013**, *6*, 1028. [[CrossRef](#)] [[PubMed](#)]
2. Li, X.; Qiao, Y.; Guo, S.; Xu, Z.; Zhu, H.; Zhang, X.; Yuan, Y.; He, P.; Ishida, M.; Zhou, H. Direct visualization of the reversible O^{2-}/O^- redox process in Li-rich cathode materials. *Adv. Mater.* **2018**, *30*, 1705197. [[CrossRef](#)]
3. Lu, Z.H.; MacNeil, D.D.; Dahn, J.R. Layered cathode materials $\text{Li}[\text{Ni}_x\text{Li}_{(1/3-2x/3)}\text{Mn}_{(2/3-x/3)}]\text{O}_2$ for lithium-ion batteries. *Electrochem. Solid State Lett.* **2001**, *4*, A191–A194. [[CrossRef](#)]
4. Lu, Z.; Beaulieu, L.Y.; Donaberger, R.A.; Thomas, C.L.; Dahn, J.R. Synthesis and electrochemical behavior of $\text{Li}[\text{Ni}_x\text{Li}_{(1/3-2x/3)}\text{Mn}_{(2/3-x/3)}]\text{O}_2$ compounds. *J. Electrochem. Soc.* **2002**, *149*, A778–A791. [[CrossRef](#)]
5. Kang, S.H.; Sun, Y.K.; Amine, K. Electrochemical and ex situ X-ray study of $\text{Li}(\text{Li}_{0.2}\text{Ni}_{0.2}\text{Mn}_{0.6})\text{O}_2$ cathode material for Li secondary batteries. *Electrochem. Solid State Lett.* **2003**, *6*, A183–A186. [[CrossRef](#)]
6. Wang, J.; He, X.; Paillard, E.; Laszczynski, N.; Li, J.; Passerini, S. Lithium- and manganese-rich oxide cathode materials for high-energy lithium ion batteries. *Adv. Energy Mater.* **2016**, *6*, 1600906. [[CrossRef](#)]
7. Gu, M.; Genc, A.; Belharouak, I.; Wang, D.; Amine, K.; Thevuthasan, S.; Baer, D.R.; Zhang, J.G.; Browning, N.D.; Liu, J.; et al. Nanoscale phase separation, cation ordering, and surface chemistry in pristine $\text{Li}_{1.2}\text{Ni}_{0.2}\text{Mn}_{0.6}\text{O}_2$ for Li-ion batteries. *Chem. Mater.* **2013**, *25*, 2319–2326. [[CrossRef](#)]
8. Hong, J.; Seo, D.H.; Kim, S.W.; Gwon, H.; Oh, S.T.; Kang, K. Structural evolution of layered $\text{Li}_{1.2}\text{Ni}_{0.2}\text{Mn}_{0.6}\text{O}_2$ upon electrochemical cycling in a Li rechargeable battery. *J. Mater. Chem.* **2010**, *20*, 10179–10186. [[CrossRef](#)]
9. Yan, P.; Nie, A.; Zheng, J.; Zhou, Y.; Lu, D.; Zhang, X.; Xu, R.; Belharouak, I.; Zu, X.; Xiao, J.; et al. Evolution of lattice structure and chemical composition of the surface reconstruction layer in $\text{Li}_{1.2}\text{Ni}_{0.2}\text{Mn}_{0.6}\text{O}_2$ cathode material for lithium ion batteries. *Nano Lett.* **2015**, *15*, 514–522. [[CrossRef](#)]
10. Hua, W.; Wang, S.; Knapp, M.; Leake, S.J.; Senyshyn, A.; Richter, C.; Yavuz, M.; Binder, J.R.; Grey, C.P.; Ehrenberg, H.; et al. Structural insights into the formation and voltage degradation of lithium- and manganese-rich layered oxides. *Nat. Commun.* **2019**, *10*, 5365. [[CrossRef](#)]
11. Zheng, J.; Gu, M.; Genc, A.; Xiao, J.; Xu, P.; Chen, X.; Zhu, Z.; Zhao, W.; Pullan, L.; Wang, C.; et al. Mitigating voltage fade in cathode materials by improving the atomic level uniformity of elemental distribution. *Nano Lett.* **2014**, *14*, 2628–2635. [[CrossRef](#)] [[PubMed](#)]
12. Qian, D.; Xu, B.; Chi, M.; Meng, Y.S. Uncovering the roles of oxygen vacancies in cation migration in lithium excess layered oxides. *Phys. Chem. Chem. Phys.* **2014**, *16*, 14665–14668. [[CrossRef](#)] [[PubMed](#)]

13. Zhang, J.; Zhang, H.; Gao, R.; Li, Z.; Hu, Z.; Liu, X. New insights into the modification mechanism of Li-rich $\text{Li}_{1.2}\text{Ni}_{0.2}\text{Mn}_{0.6}\text{O}_2$ coated by Li_2ZrO_3 . *Phys. Chem. Chem. Phys.* **2016**, *18*, 13322–13331. [[CrossRef](#)]
14. Liu, Y.; Fan, X.; Zhang, Z.; Wu, H.-H.; Liu, D.; Dou, A.; Su, M.; Zhang, Q.; Chu, D.D. Enhanced electrochemical performance of Li-rich layered cathode materials by combined Cr doping and LiAlO_2 coating. *ACS Sustain. Chem. Eng.* **2019**, *7*, 2225–2235. [[CrossRef](#)]
15. Abdel-Ghany, A.; El-Tawil, R.S.; Hashem, A.M.; Mauger, A.; Julien, C.M. Improved electrochemical performance of $\text{LiNi}_{0.5}\text{Mn}_{0.5}\text{O}_2$ by Li-enrichment and AlF_3 coating. *Materialia* **2019**, *5*, 100207. [[CrossRef](#)]
16. Lee, H.J.; Par, Y.J. Synthesis of $\text{Li}[\text{Li}_{0.2}\text{Ni}_{0.2}\text{Mn}_{0.6}]\text{O}_2$ nano-particles and their surface modification using a polydopamine layer. *J. Power Sources* **2013**, *244*, 222–233. [[CrossRef](#)]
17. Liu, Y.J.; Lv, J.; Liu, S.B.; Chen, L.; Chen, X.H. Improved electrochemical performance of $\text{Li}_{1.2}\text{Ni}_{0.2}\text{Mn}_{0.6}\text{O}_2$ cathode materials by ball milling and carbon coating. *Powder Technol.* **2013**, *239*, 461–466. [[CrossRef](#)]
18. Liu, Y.J.; Gao, Y.Y.; Lv, J.; Chen, L. A Facile method to synthesize carbon coated $\text{Li}_{1.2}\text{Ni}_{0.2}\text{Mn}_{0.6}\text{O}_2$ with improved performance. *Mater. Res. Bull.* **2013**, *48*, 4930–4934. [[CrossRef](#)]
19. Singh, G.; Thomas, R.; Kumar, A.; Katiyar, R.S.; Manivannan, A. Electrochemical and structural investigations on ZnO treated $0.5\text{Li}_2\text{MnO}_3$ - $0.5\text{LiNi}_{0.5}\text{Mn}_{0.5}\text{O}_2$ layered composite cathode material for lithium ion battery. *J. Electrochem. Soc.* **2012**, *159*, A470–A478. [[CrossRef](#)]
20. Shi, J.L.; Zhang, J.N.; He, M.; Zhang, X.D.; Yin, Y.X.; Li, H.; Guo, Y.G.; Gu, L.; Wan, L.J. Mitigating voltage decay of Li-rich cathode material via increasing Ni content for lithium-ion batteries. *ACS Appl. Mater. Interfaces* **2016**, *8*, 20138–20146. [[CrossRef](#)]
21. Uzun, D. Boron-doped $\text{Li}_{1.2}\text{Ni}_{0.2}\text{Mn}_{0.6}\text{O}_2$ as a cathode active material for lithium ion battery. *Solid State Ion.* **2015**, *281*, 73–81. [[CrossRef](#)]
22. Yamamoto, S.; Noguchi, H.; Zhao, W. Improvement of cycling performance in Ti substituted $0.5\text{Li}_2\text{MnO}_3$ - $0.5\text{LiNi}_{0.5}\text{Mn}_{0.5}\text{O}_2$ through suppressing metal dissolution. *J. Power Sources* **2015**, *278*, 76–86. [[CrossRef](#)]
23. Wang, C.C.; Manthiram, A. Influence of cationic substitutions on the first charge and reversible capacities of lithium-rich layered oxide cathodes. *J. Mater. Chem. A* **2013**, *1*, 10209–10217. [[CrossRef](#)]
24. Li, J.; Nie, A.; Zhan, C.; Lu, J.; Yuan, Y.; Shahbazian-Yassar, R.; Qiu, X.; Amine, K. Improve first-cycle efficiency and rate performance of layered-layered $\text{Li}_{1.2}\text{Mn}_{0.6}\text{Ni}_{0.2}\text{O}_2$ using oxygen stabilizing dopant. *ACS Appl. Mater. Interfaces* **2015**, *7*, 16040–16045. [[CrossRef](#)] [[PubMed](#)]
25. Zhuang, Y.; Du, F.; Zhu, L.; Cao, H.; Dai, H.; Adkins, J.; Zhou, Q.; Zheng, J. Trimethylsilyl (trimethylsiloxy) acetate as a novel electrolyte additive for improvement of electrochemical performance of lithium-rich $\text{Li}_{1.2}\text{Ni}_{0.2}\text{Mn}_{0.6}\text{O}_2$ cathode in lithium-ion batteries. *Electrochim. Acta* **2018**, *290*, 220–227. [[CrossRef](#)]
26. Wang, C.C.; Lin, Y.C.; Chou, P.H. Mitigation of layer to spinel conversion of a lithium rich layered oxide cathode by substitution of Al in a lithium ion battery. *RSC Adv.* **2015**, *5*, 68919–68928. [[CrossRef](#)]
27. Wang, D.; Huang, Y.; Huo, Z.; Chen, L. Synthesize and electrochemical characterization of Mg-doped Li-rich layered $\text{Li}[\text{Li}_{0.2}\text{Ni}_{0.2}\text{Mn}_{0.6}]\text{O}_2$ cathode material. *Electrochim. Acta* **2013**, *107*, 461–466. [[CrossRef](#)]
28. Huang, J.-X.; Li, B.; Liu, B.; Liu, B.-J.; Zhao, J.-B.; Ren, B. Structural evolution of NM (Ni and Mn) lithium-rich layered material revealed by in-situ electrochemical Raman spectroscopic study. *J. Power Sources* **2016**, *310*, 85–90. [[CrossRef](#)]
29. Liu, Y.; Fan, X.; Huang, X.; Liu, D.; Dou, A.; Su, M.; Chu, D. Electrochemical performance of $\text{Li}_{1.2}\text{Ni}_{0.2}\text{Mn}_{0.6}\text{O}_2$ coated with a facilely synthesized $\text{Li}_{1.3}\text{Al}_{0.3}\text{Ti}_{1.7}(\text{PO}_4)_3$. *J. Power Sources* **2018**, *403*, 27–37. [[CrossRef](#)]
30. Zhong, Z.; Ye, N.; Wang, H.; Ma, Z. Low temperature combustion synthesis and performance of spherical $0.5\text{Li}_2\text{MnO}_3$ - $\text{LiNi}_{0.5}\text{Mn}_{0.5}\text{O}_2$ cathode material for Li-ion batteries. *Chem. Eng. J.* **2011**, *175*, 579–584. [[CrossRef](#)]
31. Zhang, Q.; Mei, J.; Xie, X.; Wang, X.; Zhang, J. Solution combustion synthesis and enhanced electrochemical performance $\text{Li}_{1.2}\text{Ni}_{0.2}\text{Mn}_{0.6}\text{O}_2$ nanoparticles by controlling $\text{NO}_3^-/\text{CH}_3\text{COO}^-$ ratio of the precursors. *Mater. Res. Bull.* **2015**, *70*, 397–402. [[CrossRef](#)]
32. Yang, P.; Li, H.; Wei, X.; Zhang, S.; Xing, Y. Structure tuned $\text{Li}_{1.2}\text{Mn}_{0.6}\text{Ni}_{0.2}\text{O}_2$ with low cation mixing and Ni segregation as high performance cathode materials for Li-ion batteries. *Electrochim. Acta* **2018**, *271*, 276–283. [[CrossRef](#)]
33. Liu, Y.; Liu, D.; Wu, H.-H.; Fan, X.; Dou, A.; Zhang, Q.; Su, M. Improved cycling stability of Na-doped cathode materials $\text{Li}_{1.2}\text{Ni}_{0.2}\text{Mn}_{0.6}\text{O}_2$ via a facile synthesis. *ACS Sustain. Chem. Eng.* **2018**, *6*, 13045–13055. [[CrossRef](#)]

34. He, X.; Wang, J.; Wang, L.; Li, J. Nano-crystalline $\text{Li}_{1.2}\text{Mn}_{0.6}\text{Ni}_{0.2}\text{O}_2$ prepared via amorphous complex precursor and its electrochemical performances as cathode material for Lithium-ion batteries. *Materials* **2016**, *9*, 661. [[CrossRef](#)] [[PubMed](#)]
35. Liu, J.; Chen, H.; Xie, J.; Sun, Z.; Wu, N.; Wu, B. Electrochemical performance studies of Li-rich cathode materials with different primary particle sizes. *J. Power Sources* **2014**, *251*, 208–214. [[CrossRef](#)]
36. Zhang, L.; Wu, B.; Li, N.; Mu, D.; Zhang, C.; Wu, F. Rod-like hierarchical nano/micro $\text{Li}_{1.2}\text{Ni}_{0.2}\text{Mn}_{0.6}\text{O}_2$ as high performance cathode materials for lithium-ion batteries. *J. Power Sources* **2013**, *240*, 644–652. [[CrossRef](#)]
37. Zhao, T.; Gao, X.; Wei, Z.; Guo, K.; Wu, F.; Li, L.; Chen, R. Three-dimensional $\text{Li}_{1.2}\text{Ni}_{0.2}\text{Mn}_{0.6}\text{O}_2$ cathode materials synthesized by a novel hydrothermal method for lithium-ion batteries. *J. Alloy. Compd.* **2018**, *757*, 16–23. [[CrossRef](#)]
38. Li, L.; Wang, L.; Zhang, X.; Xue, Q.; Wei, L.; Wu, F.; Chen, R. 3D reticular $\text{Li}_{1.2}\text{Ni}_{0.2}\text{Mn}_{0.6}\text{O}_2$ cathode material for lithium-ion batteries. *ACS Appl. Mater. Interfaces* **2017**, *9*, 1516–1523. [[CrossRef](#)]
39. Yang, P.; Wang, W.; Zhang, X.; Li, H.; Zhang, S.; Xing, Y. Self-standing $\text{Li}_{1.2}\text{Mn}_{0.6}\text{Ni}_{0.2}\text{O}_2$ /graphene membrane as a binder-free cathode for Li-ion batteries. *RSC Adv.* **2018**, *8*, 39769–39776.
40. Hao, R.; Liang, J.; Yang, Z.; Liang, C.; Cuan, X.; Gao, A.; Chen, H. Synthesis and Investigation of the nanocrystalline $\text{Li}_{1.2}\text{Ni}_{0.2}\text{Mn}_{0.6}\text{O}_2$ cathodes for Li-ion batteries by using ultrasonic/microwave-assisted co-precipitation method with different ultrasonic time. *J. South China Norm. Univ.* **2017**, *49*, 6–10.
41. Wang, H.; Li, X.; Zhou, Q.; Ming, H.; Adkins, J.; Jin, L.; Jia, Z.; Fu, Y.; Zheng, J. Diversified $\text{Li}_{1.2}\text{Ni}_{0.2}\text{Mn}_{0.6}\text{O}_2$ nanoparticles from birnessite towards application specificity and enhancement in lithium-ion batteries. *J. Alloy. Compd.* **2014**, *604*, 217–225. [[CrossRef](#)]
42. Sun, L.; Yi, X.; Shi, C.; Ren, X.; Gao, Y.; Li, Y.; Zhang, P. A Li-rich $\text{Li}[\text{Li}_{0.2}\text{Ni}_{0.2}\text{Mn}_{0.6}]\text{O}_2$ cathode material in situ coated with polyaniline. *Int. J. Electrochem. Sci.* **2017**, *12*, 4756–4767. [[CrossRef](#)]
43. Liu, Y.; Zhang, Z.; Fu, Y.; Wang, Q.; Pan, J.; Su, M.; Battaglia, V.S. Investigation the electrochemical performance of $\text{Li}_{1.2}\text{Ni}_{0.2}\text{Mn}_{0.6}\text{O}_2$ cathode material with ZnAl_2O_4 coating for lithium ion batteries. *J. Alloy. Compd.* **2016**, *685*, 523–532. [[CrossRef](#)]
44. Lin, J.; Mu, D.; Jin, Y.; Wu, B.; Wu, F. Li-rich layered composite $\text{Li}[\text{Li}_{0.2}\text{Ni}_{0.2}\text{Mn}_{0.6}]\text{O}_2$ synthesized by a novel approach as cathode material for lithium ion battery. *J. Power Sources* **2013**, *230*, 76–80. [[CrossRef](#)]
45. Lee, D.K.; Park, S.H.; Amine, K.; Bang, H.J.; Parakash, J.; Sun, Y.-K. High capacity $\text{Li}[\text{Li}_{0.2}\text{Ni}_{0.2}\text{Mn}_{0.6}]\text{O}_2$ cathode materials via a carbonate co-precipitation method. *J. Power Sources* **2006**, *162*, 1346–1350. [[CrossRef](#)]
46. Barrett, E.P.; Joyner, L.G.; Halenda, P.P. The determination of pore volume and area distributions in porous substances. I. Computations from nitrogen isotherms. *J. Am. Chem. Soc.* **1951**, *73*, 373–380. [[CrossRef](#)]
47. Wang, G.; Xie, J.; Cao, G.; Zhu, T.; Zhao, X.; Zhang, S. Electrochemical performance of $0.5\text{Li}_2\text{MnO}_3$ - $0.5\text{LiNi}_{0.5}\text{Mn}_{0.5}\text{O}_2$ nanotubes prepared by a self-templating route. *ECS Electrochem. Lett.* **2013**, *2*, A98–A101. [[CrossRef](#)]
48. Li, G.R.; Feng, X.; Ding, Y.; Ye, S.H.; Gao, X.P. AlF-coated $\text{Li}(\text{Li}_{0.17}\text{Ni}_{0.25}\text{Mn}_{0.58})\text{O}_2$ as cathode material for Li-ion batteries. *Electrochim. Acta* **2012**, *78*, 308–315. [[CrossRef](#)]
49. Yang, K.; Fan, L.Z.; Guo, J.; Qu, X.H. Significant improvement of electrochemical properties of AlF_3 -coated $\text{LiNi}_{0.5}\text{Co}_{0.2}\text{Mn}_{0.3}\text{O}_2$ cathode materials. *Electrochim. Acta* **2012**, *63*, 363–368. [[CrossRef](#)]
50. Wu, F.; Lu, H.Q.; Su, Y.F.; Li, N.; Bao, L.Y.; Chen, S. Preparation and electrochemical performance of Li-rich layered cathode material, $\text{Li}(\text{Ni}_{0.2}\text{Li}_{0.2}\text{Mn}_{0.6})\text{O}_2$ for lithium-ion batteries. *J. Appl. Electrochem.* **2010**, *40*, 783–789. [[CrossRef](#)]
51. Zhao, T.; Li, L.; Chen, R.; Wu, H.; Zhang, X.; Chen, S.; Xie, M.; Wu, F.; Lu, J.; Amine, K. Design of surface protective layer of LiF/FeF_3 nanoparticles in Li-rich cathode for high-capacity Li-ion batteries. *Nano Energy* **2015**, *15*, 164–176. [[CrossRef](#)]
52. Shannon, R.D. Revised effective ionic radii and systematic studies of interatomic distances in halides and chalcogenides. *Acta Cryst. A* **1976**, *32*, 751–767. [[CrossRef](#)]
53. Chong, S.; Liu, Y.; Yan, W.; Chen, Y. Effect of valence states of Ni and Mn on the structural and electrochemical properties of $\text{Li}_{1.2}\text{Ni}_x\text{Mn}_{0.8-x}\text{O}_2$ cathode materials for lithium-ion batteries. *RSC Adv.* **2016**, *6*, 53662–53668. [[CrossRef](#)]
54. Ohzuku, T.; Ueda, A.; Nagayama, M. Electrochemistry and structural chemistry of LiNiO_2 (R-3m) for 4 volt secondary lithium cells. *J. Electrochem. Soc.* **1993**, *140*, 1862–1870. [[CrossRef](#)]
55. Dahn, J.R.; von Sacken, U.; Michal, C.A. Structure and electrochemistry of $\text{Li}_{1-y}\text{NiO}_2$ and a new Li_2NiO_2 phase with the $\text{Ni}(\text{OH})_2$ structure. *Solid State Ion.* **1990**, *44*, 87–97. [[CrossRef](#)]

56. Reimers, J.N.; Rossen, E.; Jones, C.D.; Dahn, J.R. Structure and electrochemistry of $\text{Li}_x\text{Fe}_y\text{Ni}_{1-y}\text{O}_2$. *Solid State Ion.* **1993**, *61*, 335–344. [CrossRef]
57. Hashem, A.M.; Abdel-Ghany, A.E.; Scheuermann, M.; Indris, S.; Ehrenberg, H.; Mauger, A.; Julien, C.M. Doped nanoscale NMC333 cathode materials for Li-ion batteries. *Materials* **2019**, *12*, 2899. [CrossRef]
58. Singer, A.; Zhang, M.; Hy, S.; Cela, D.; Fang, C.; Wynn, T.A.; Qiu, B.; Xia, Y.; Liu, Z.; Ulvestad, A.; et al. Nucleation of dislocations and their dynamics in layered oxide cathode materials during battery charging. *Nat. Energy* **2018**, *3*, 641–647. [CrossRef]
59. Li, Y.; Wu, C.; Bai, Y.; Liu, L.; Wang, H.; Wu, F.; Zhang, N.; Zou, Y. Hierarchical mesoporous lithium-rich $\text{Li}[\text{Li}_{0.2}\text{Ni}_{0.2}\text{Mn}_{0.6}]\text{O}_2$ cathode material synthesized via ice templating for lithium-ion battery. *ACS Appl. Mater. Interfaces* **2016**, *8*, 18832–18840. [CrossRef]
60. Poyraz, A.S.; Kuo, C.-H.; Biswas, S.; King'onde, C.K.; Suib, S.L. A general approach to crystalline and monomodal pore size mesoporous materials. *Nat. Commun.* **2013**, *4*, 2952. [CrossRef]
61. Chang, C.; Dong, J.; Guan, L.; Zhang, D. Enhanced electrochemical performance of $\text{Li}_{1.27}\text{Cr}_{0.2}\text{Mn}_{0.53}\text{O}_2$ layered cathode materials via a nanomilling-assisted solid-state process. *Materials* **2019**, *12*, 468. [CrossRef]
62. Xiang, Y.; Sun, Z.; Li, J.; Wu, X.; Liu, Z.; Xiong, L.; He, Z.; Long, B.; Chen Yang, C.; Yin, Z. Improved electrochemical performance of $\text{Li}_{1.2}\text{Ni}_{0.2}\text{Mn}_{0.6}\text{O}_2$ cathode material for lithium ion batteries synthesized by the polyvinyl alcohol assisted sol-gel method. *Ceram. Int.* **2017**, *43*, 2320–2324. [CrossRef]
63. Zhang, M.; Liu, H.; Liu, Z.; Fang, C.; Meng, Y.S. Modified coprecipitation synthesis of mesostructure-controlled Li rich layered oxides for minimizing voltage degradation. *ACS Energy Mater.* **2018**, *1*, 3369–3376. [CrossRef]
64. Thiele, G.; Poston, M.; Brown, R. A Case Study in Sizing Nanoparticles. Micromeritics Instrument Corporation. Available online: <http://www.particletesting.com/library> (accessed on 1 January 2019).
65. Li, Z.E.; Du, F.; Bie, X.; Zhang, D.; Cai, Y.; Cui, X.; Wang, C.; Chen, G.; Wei, Y. Electrochemical kinetics of the $\text{Li}[\text{Li}_{0.23}\text{Co}_{0.3}\text{Mn}_{0.47}]\text{O}_2$ cathode material studied by GITT and EIS. *J. Phys. Chem. C* **2010**, *114*, 22751–22757. [CrossRef]
66. Lu, Z.; Dahn, J.R. Understanding the anomalous capacity of $\text{Li}/\text{Li}[\text{Ni}_x\text{Li}_{(1/3-2x/3)}\text{Mn}_{(2/3-x/3)}]\text{O}_2$ cells using in situ X-ray diffraction and electrochemical studies. *J. Electrochem. Soc.* **2002**, *149*, A815–A822. [CrossRef]
67. Thackeray, M.M.; Kang, S.-H.; Johnson, C.S.; Vaughey, J.T.; Hackney, S.A. Comments on the structural complexity of lithium-rich $\text{Li}_{1+x}\text{M}_{1-x}\text{O}_2$ electrodes (M = Mn, Ni, Co) for lithium batteries. *Electrochem. Commun.* **2006**, *8*, 1531–1538. [CrossRef]
68. Yu, H.; Wang, Y.; Asakura, D.; Hosono, E.; Zhang, T.; Zhou, H. Electrochemical kinetics of the $0.5\text{Li}_2\text{MnO}_3\text{-}0.5\text{LiMn}_{0.42}\text{Ni}_{0.42}\text{Co}_{0.16}\text{O}_2$ “composite” layered cathode material for lithium-ion batteries. *RSC Adv.* **2012**, *2*, 8797–8807. [CrossRef]
69. Julien, C. Local cationic environment in lithium nickel-cobalt oxides used as cathode materials for lithium batteries. *Solid State Ion.* **2000**, *136–137*, 887–896. [CrossRef]
70. Abdel-Ghany, A.; Zaghib, K.; Julien, C.M. The layered $\text{LiNi}_0.5\text{Mn}_0.5\text{O}_2$ positive electrode material for Li-ion battery. In *Portable Emergency Energy Sources from Materials to Systems*; Stoyanov, Z., Vladikova, D., Eds.; Prof. Martin Drinov Academic Publishing House of BAS: Sofia, Bulgaria, 2006; pp. 1–36.
71. Julien, C.M.; Massot, M. Lattice vibrations of materials for lithium rechargeable batteries. III. Lithium manganese oxides. *Mater. Sci. Eng. B* **2003**, *100*, 69–78. [CrossRef]
72. Sun, Y.K.; Lee, M.J.; Yoon, C.S.; Hassoun, J.; Amine, K.; Scrosati, B. The role of AlF_3 coatings in improving electrochemical cycling of Li-enriched nickel-manganese oxide electrodes for Li-ion batteries. *Adv. Mater.* **2012**, *24*, 1192–1196. [CrossRef] [PubMed]
73. Hwang, B.-J.; Wang, C.-J.; Chen, C.-H.; Tsai, Y.-W.; Venkateswarlu, M. Electrochemical properties of $\text{Li}[\text{Ni}_x\text{Li}_{(1-2x)/3}\text{Mn}_{(2-x)/3}]\text{O}_2$ ($0 \leq x \leq 0.5$) cathode materials prepared by a sol-gel process. *J. Power Sources* **2005**, *146*, 658–663. [CrossRef]
74. Mohanty, D.; Sefat, A.S.; Kalnaus, S.; Li, J.; Meisner, R.A.; Payzant, E.A.; Abraham, D.P.; Wood, D.L.; Daniel, C. Investigating phase transformation in the $\text{Li}_{1.2}\text{Co}_{0.1}\text{Mn}_{0.55}\text{Ni}_{0.15}\text{O}_2$ lithium-ion battery cathode during high-voltage hold (4.5 V) via magnetic, X-ray diffraction and electron microscopy studies. *J. Mater. Chem. A* **2013**, *1*, 6249–6261. [CrossRef]
75. Song, B.; Lai, M.O.; Lu, L. Influence of Ru substitution on Li-rich $0.55\text{Li}_2\text{MnO}_3\text{-}0.45\text{LiNi}_{1/3}\text{Co}_{1/3}\text{Mn}_{1/3}\text{O}_2$ cathode for Li-ion batteries. *Electrochim. Acta* **2012**, *80*, 187–195. [CrossRef]

76. Li, X.; Xin, H.; Liu, Y.; Li, D.; Yuan, X.; Qin, X. Effect of niobium doping on the microstructure and electrochemical properties of lithium-rich layered $\text{Li}[\text{Li}_{0.2}\text{Ni}_{0.2}\text{Mn}_{0.6}]\text{O}_2$ as cathode materials for lithium ion batteries. *RSC Adv.* **2015**, *5*, 45351–45358. [[CrossRef](#)]
77. Zheng, J.M.; Zhang, Z.R.; Wu, X.B.; Dong, Z.X.; Zhu, Z.; Yang, Y. The effects of AlF_3 coating on the performance of $\text{Li}[\text{Li}_{0.2}\text{Mn}_{0.54}\text{Ni}_{0.13}\text{Co}_{0.13}]\text{O}_2$ positive electrode material for lithium-ion battery. *J. Electrochem. Soc.* **2008**, *155*, A775–A782. [[CrossRef](#)]
78. Xiang, X.; Li, W. Self-directed chemical synthesis of lithium-rich layered oxide $\text{Li}[\text{Li}_{0.2}\text{Ni}_{0.2}\text{Mn}_{0.6}]\text{O}_2$ with tightly interconnected particles as cathode of lithium ion batteries with improved rate capability. *Electrochim. Acta* **2014**, *127*, 259–265. [[CrossRef](#)]
79. Armstrong, A.R.; Holzapfel, M.; Novak, P.; Johnson, C.S.; Kang, S.; Thackeray, M.M.; Bruce, P.G. Demonstrating oxygen loss and associated structural reorganization in the lithium battery cathode $\text{Li}[\text{Li}_{0.2}\text{Ni}_{0.2}\text{Mn}_{0.6}]\text{O}_2$. *J. Am. Chem. Soc.* **2006**, *128*, 8694–8698. [[CrossRef](#)]
80. Hy, S.; Su, W.N.; Chen, J.M.; Hwang, B.J. Soft X-ray absorption spectroscopy and Raman study on $\text{Li}_{1.2}\text{Ni}_{0.2}\text{Mn}_{0.6}\text{O}_2$ for lithium-ion batteries. *J. Phys. Chem. C* **2012**, *116*, 25242–25247. [[CrossRef](#)]
81. Guan, X.T.; Ding, B.; Liu, X.F.; Zhu, J.J.; Mi, C.H.; Zhang, X.G. Enhancing the electrochemical performance of $\text{Li}_{1.2}\text{Ni}_{0.2}\text{Mn}_{0.6}\text{O}_2$ by surface modification with nickel-manganese composite oxide. *J. Solid State Electrochem.* **2013**, *17*, 2087–2093. [[CrossRef](#)]
82. Chen, L.; Su, Y.F.; Chen, S.; Li, N.; Bao, L.Y.; Li, W.K.; Wang, Z.; Wang, M.; Wu, F. Hierarchical $\text{Li}_{1.2}\text{Ni}_{0.2}\text{Mn}_{0.6}\text{O}_2$ nanoplates with exposed {010} planes as high-performance cathode material for lithium-ion batteries. *Adv. Mater.* **2014**, *26*, 6756–6760. [[CrossRef](#)]
83. Nayak, P.K.; Grinblat, J.; Levi, M.; Aurbach, D. Electrochemical and structural characterization of carbon coated $\text{Li}_{1.2}\text{Mn}_{0.56}\text{Ni}_{0.16}\text{Co}_{0.08}\text{O}_2$ and $\text{Li}_{1.2}\text{Mn}_{0.6}\text{Ni}_{0.2}\text{O}_2$ as cathode materials for Li-ion batteries. *Electrochim. Acta* **2014**, *137*, 546–556. [[CrossRef](#)]
84. Ho, C.; Raistrick, I.D.; Huggins, R.A. Application of a-c techniques to the study of lithium diffusion in tungsten trioxide thin films. *J. Electrochem. Soc.* **1980**, *127*, 343–350. [[CrossRef](#)]
85. Bard, A.J.; Faulkner, L.R. *Electrochemical Methods: Fundamentals and Applications*; John Wiley & Sons Inc.: New York, NY, USA, 2001; pp. 226–260.
86. Sasakawa, T.; Harada, Y.; Takami, N.; Kitamura, N.; Idemoto, Y. Influence of initial charge condition on structural stability and electrochemical properties of $\text{Li}_{1.2}\text{Ni}_{0.2}\text{Mn}_{0.6}\text{O}_2$ cathode materials. *Electrochim. Acta* **2015**, *174*, 406–410. [[CrossRef](#)]
87. Xiao, P.; Lv, T.; Chen, X.; Chang, C. $\text{LiNi}_{0.8}\text{Co}_{0.15}\text{Al}_{0.05}\text{O}_2$ enhanced electrochemical performance from reduced cationic disordering in Li slab. *Sci. Rep.* **2017**, *7*, 1408. [[CrossRef](#)] [[PubMed](#)]
88. Ku, K.; Kim, B.; Jung, S.-K.; Gong, Y.; Eum, D.; Yoon, G.; Park, K.; Hong, J.; Cho, S.-P.; Kim, D.-H.; et al. A new lithium diffusion model in layered oxides based on asymmetric but reversible transition metal migration. *Energy Environ. Sci.* **2020**, *13*, 1269–1278. [[CrossRef](#)]
89. Julien, C.M.; Mauger, A. In situ Raman analyses of electrode materials for Li-ion batteries. *AIMS Mater. Sci.* **2018**, *5*, 650–698. [[CrossRef](#)]
90. Lin, M.-H.; Cheng, J.-H.; Huang, H.-F.; Chen, U.-F.; Huang, C.-M.; Hsieh, H.-W.; Lee, J.-M.; Chen, J.-M.; Su, W.-N.; Hwang, B.-J. Revealing the mitigation of intrinsic structure transformation and oxygen evolution in a layered $\text{Li}_{1.2}\text{Ni}_{0.2}\text{Mn}_{0.6}\text{O}_2$ cathode using restricted charging protocols. *J. Power Sources* **2017**, *359*, 539–548. [[CrossRef](#)]
91. Julien, C.M.; Mauger, A. Functional behavior of AlF_3 coatings for high-performance cathode materials for lithium-ion batteries. *AIMS Mater. Sci.* **2019**, *6*, 406–440. [[CrossRef](#)]
92. Vetter, J.; Novák, P.; Wagner, M.R.; Veit, C.; Möller, K.-C.; Besenhard, J.O.; Winter, M.; Wohlfahrt-Mehrens, M.; Vogler, C.; Hammouche, A. Ageing mechanisms in lithium-ion batteries. *J. Power Sources* **2005**, *147*, 269–281. [[CrossRef](#)]
93. Tröltzsch, U.; Kanoun, O.; Tränkler, H.R. Characterizing aging effects of lithium ion batteries by impedance spectroscopy. *Electrochim. Acta* **2006**, *51*, 1664–1672. [[CrossRef](#)]
94. Kiziltas-Yavuz, N.; Herklotz, M.; Hashem, A.M.; Abuzeid, H.M.; Schwarz, B.; Ehrenberg, H.; Mauger, A.; Julien, C.M. Synthesis, structural, magnetic and electrochemical properties of $\text{LiNi}_{1/3}\text{Mn}_{1/3}\text{Co}_{1/3}\text{O}_2$ prepared by a sol-gel method using table sugar as chelating agent. *Electrochim. Acta* **2013**, *113*, 313–321. [[CrossRef](#)]
95. Birkl, C.R.; Roberts, M.R.; McTurk, E.; Bruce, P.G.; Howey, D.A. Degradation diagnostics for lithium ion cells. *J. Power Sources* **2017**, *341*, 373–386. [[CrossRef](#)]

96. Cabana, J.; Kwon, B.J.; Hu, L. Mechanisms of degradation and strategies for the stabilization of cathode–electrolyte interfaces in Li-ion batteries. *Acc. Chem. Res.* **2018**, *51*, 299–308. [[CrossRef](#)] [[PubMed](#)]
97. Xu, Z.; Rahman, M.M.; Mu, L.; Liu, L.; Lin, F. Chemomechanical behaviors of layered cathode materials in alkali metal ion batteries. *J. Mater. Chem. A* **2018**, *6*, 21859–21884. [[CrossRef](#)]
98. Zheng, J.M.; Gu, M.; Xiao, J.; Polzin, B.J.; Yan, P.; Chen, X.; Wang, C.; Zhang, J.-G. Functioning mechanism of AlF₃ coating on the Li- and Mn-rich cathode materials. *Chem. Mater.* **2014**, *26*, 6320–6327. [[CrossRef](#)]
99. Deng, H.; Belharouak, I.; Yoon, C.S.; Sun, Y.-K.; Amine, K. High temperature performance of surface-treated Li_{1.1}(Ni_{0.15}Co_{0.1}Mn_{0.55})O_{1.95} layered oxide. *J. Electrochem. Soc.* **2010**, *157*, A1035–A1039. [[CrossRef](#)]
100. Kang, S.H.; Thackeray, M.M. Enhancing the rate capability of high capacity $x\text{Li}_2\text{MnO}_3 \cdot (1-x)\text{LiMO}_2$ (M = Mn, Ni, Co) electrodes by Li–Ni–PO₄ treatment. *Electrochem. Commun.* **2009**, *11*, 748–751. [[CrossRef](#)]
101. Liu, H.; Chen, C.; Du, C.Y.; He, X.S.; Yin, G.P.; Song, B.; Zuo, P.J.; Cheng, X.Q.; Ma, Y.L.; Gao, Y.Z. Lithium-rich Li_{1.2}Ni_{0.13}Co_{0.13}Mn_{0.54}O₂ oxide coated by Li₃PO₄ and carbon nanocomposite layers as high performance cathode materials for lithium ion batteries. *J. Mater. Chem. A* **2015**, *3*, 2634–2641. [[CrossRef](#)]
102. Lee, Y.; Lee, J.; Lee, K.Y.; Mun, J.; Lee, J.K.; Choi, W. Facile formation of a Li₃PO₄ coating layer during the synthesis of a lithium-rich layered oxide for high-capacity lithium-ion batteries. *J. Power Sources* **2016**, *315*, 284–293. [[CrossRef](#)]
103. Chen, D.; Zheng, F.; Li, L.; Chen, M.; Zhong, X.; Li, W.; Lu, L. Effect of Li₃PO₄ coating of layered lithium-rich oxide on electrochemical performance. *J. Power Sources* **2017**, *34*, 1147–1155. [[CrossRef](#)]
104. Shaw, L.; Ashuri, M. Coating—A potent method to enhance electrochemical performance of Li(Ni_xMn_yCo_z)O₂ cathodes for Li-ion batteries. *Adv. Mater. Lett.* **2019**, *10*, 369–380.
105. Sahni, K.; Ashuri, M.; He, Q.; Sahore, R.; Bloom, I.D.; Liu, Y.; Kaduk, J.A.; Shaw, L.L. H₃PO₄ treatment to enhance the electrochemical properties of Li(Ni_{1/3}Mn_{1/3}Co_{1/3})O₂ and Li(Ni_{0.5}Mn_{0.3}Co_{0.2})O₂ cathodes. *Electrochim. Acta* **2019**, *301*, 8–22. [[CrossRef](#)]
106. Ashuri, M.; He, Q.; Shi, Z.; Chen, C.; Yao, W.; Kaduk, J.; Segre, C.; Shaw, L. Long-term cycle behavior of nano-LiCoO₂ and its postmortem analysis. *J. Phys. Chem. C* **2019**, *123*, 3299–3308. [[CrossRef](#)]
107. Chen, C.; Yao, W.; He, Q.; Ashuri, M.; Kaduk, J.; Liu, Y.; Shaw, L. Tunable LiAlO₂/Al₂O₃ coating through a wet-chemical method to improve stability of nano-LiCoO₂. *ACS Appl. Energy Mater.* **2019**, *2*, 3098–3113. [[CrossRef](#)]
108. Lee, E.-S.; Huq, A.; Chang, H.-Y.; Manthiram, A. High-voltage, high-energy layered-spinel composite cathodes with superior cycle life for lithium-ion batteries. *Chem. Mater.* **2012**, *24*, 600–612. [[CrossRef](#)]
109. Lee, E.-S.; Huq, A.; Manthiram, A. Understanding the effect of synthesis temperature on the structural and electrochemical characteristics of layered-spinel composite cathodes for lithium-ion batteries. *J. Power Sources* **2013**, *240*, 193–203. [[CrossRef](#)]
110. Zhang, X.; Meng, X.; Elam, J.W.; Belharouak, I. Electrochemical characterization of voltage fade of Li_{1.2}Ni_{0.2}Mn_{0.6}O₂ cathode. *Solid State Ion.* **2014**, *268*, 231–235. [[CrossRef](#)]
111. Lee, E.-S.; Manthiram, A. Smart design of lithium-rich layered oxide cathode compositions with suppressed voltage decay. *J. Mater. Chem. A* **2014**, *2*, 3932–3939. [[CrossRef](#)]
112. Xu, B.; Fell, C.R.; Chi, M.; Meng, Y.S. Identifying surface structural changes in layered Li-excess nickel manganese oxides in high voltage lithium ion batteries: A joint experimental and theoretical study. *Energy Environ. Sci.* **2011**, *4*, 2223–2233. [[CrossRef](#)]
113. Li, Q.; Li, G.; Fu, C.; Luo, D.; Fan, J.; Li, L. K⁺-Doped Li_{1.2}Mn_{0.54}Co_{0.13}Ni_{0.13}O₂: A novel cathode material with an enhanced cycling stability for lithium-ion batteries. *ACS Appl. Mater. Interfaces* **2014**, *6*, 10330–10341. [[CrossRef](#)]
114. Chong, S.; Wu, Y.; Chen, Y.; Shu, C.; Liu, Y. A strategy of constructing spherical core-shell structure of Li_{1.2}Ni_{0.2}Mn_{0.6}O₂@Li_{1.2}Ni_{0.4}Mn_{0.4}O₂ cathode material for high-performance lithium-ion batteries. *J. Power Sources* **2017**, *356*, 153–162. [[CrossRef](#)]
115. Ding, X.; Luo, D.; Cui, J.; Xie, H.; Ren, Q.; Lin, Z. An ultra-long-life lithium-rich Li_{1.2}Mn_{0.6}Ni_{0.2}O₂ cathode by three-in-one surface modification for lithium-ion batteries. *Angew. Chem. Int. Ed.* **2020**. [[CrossRef](#)]

